Measuring small compartment dimensions by probing diffusion dynamics via Non-uniform Oscillating-Gradient Spin-Echo (NOGSE) NMR

Noam Shemesh, Gonzalo A. Álvarez, Lucio Frydman*

Department of Chemical Physics, Weizmann Institute of Science, Rehovot, 76100, Israel

*Correspondence to:

Prof. Lucio Frydman

Department of Chemical Physics, Weizmann Institute of Science, Rehovot 76100, Israel.

Tel: 972-8-9342024.

Fax: 972-8-9344123

E-mail: lucio.frydman@weizmann.ac.il

Running title: *Compartment dimensions via NOGSE NMR*

Abstract

Noninvasive measurements of microstructure in materials, cells, and in biological tissues, constitute a unique capability of gradient-assisted NMR. Diffusion-diffraction MR approaches pioneered by Callaghan demonstrated this ability; Oscillating-Gradient Spin-Echo (OGSE) methodologies tackle the demanding gradient amplitudes required for observing diffraction patterns by utilizing constant-frequency oscillating gradient pairs that probe the diffusion spectrum, $D(\omega)$. Here we present a new class of diffusion MR experiments, termed Non-uniform Oscillating-Gradient Spin-Echo (NOGSE), which dynamically probe multiple frequencies of the diffusion spectral density at once, thus affording direct microstructural information on the compartment's dimension. The NOGSE methodology applies N constant-amplitude gradient oscillations; N-1 of these oscillations are spaced by a characteristic time x, followed by a single gradient oscillation characterized by a time y, such that the diffusion dynamics is probed while keeping $(N-1)x+y\equiv T_{NOGSE}$ constant. These constant-time, fixed-gradient-amplitude, multi-frequency attributes render NOGSE particularly useful for probing small compartment dimensions with relatively weak gradients whilst alleviating difficulties associated with probing $D(\omega)$ element-by-element as done in conventional OGSE, or with varying relaxation weightings associated with other temporally-dependent diffusion experiments. Analytical descriptions of the NOGSE signal are given, and the sequence's ability to extract small compartment sizes is demonstrated using a microstructural phantom. Excellent agreement between theory and experiments was evidenced even upon applying weak gradient amplitudes. An MR imaging version of NOGSE was also implemented in *ex-vivo* pig spinal cords and mouse brains, affording maps based on compartment sizes. The effects of size distributions on NOGSE are also briefly analyzed.

Keywords: Restricted diffusion, Oscillating Gradients, OGSE, Microstructure, Magnetic Resonance Imaging, CNS, gradient echoes, selective dynamical recoupling.

Abbreviations: Apparent Diffusion Coefficient (ADC), Carr-Purcell-Meiboom-Gill (CPMG), Diffusion Tensor Imaging (DTI), Fourier Transform (FT), Gray Matter (GM), Non-uniform Oscillating-Gradient Spin-Echo (NOGSE), Oscillating-Gradient Spin-Echo (OGSE), Pulsed-Gradient Spin-Echo (PGSE), Selective Dynamical Recoupling (SDR), White Matter (WM).

TOC Graphical Abstract

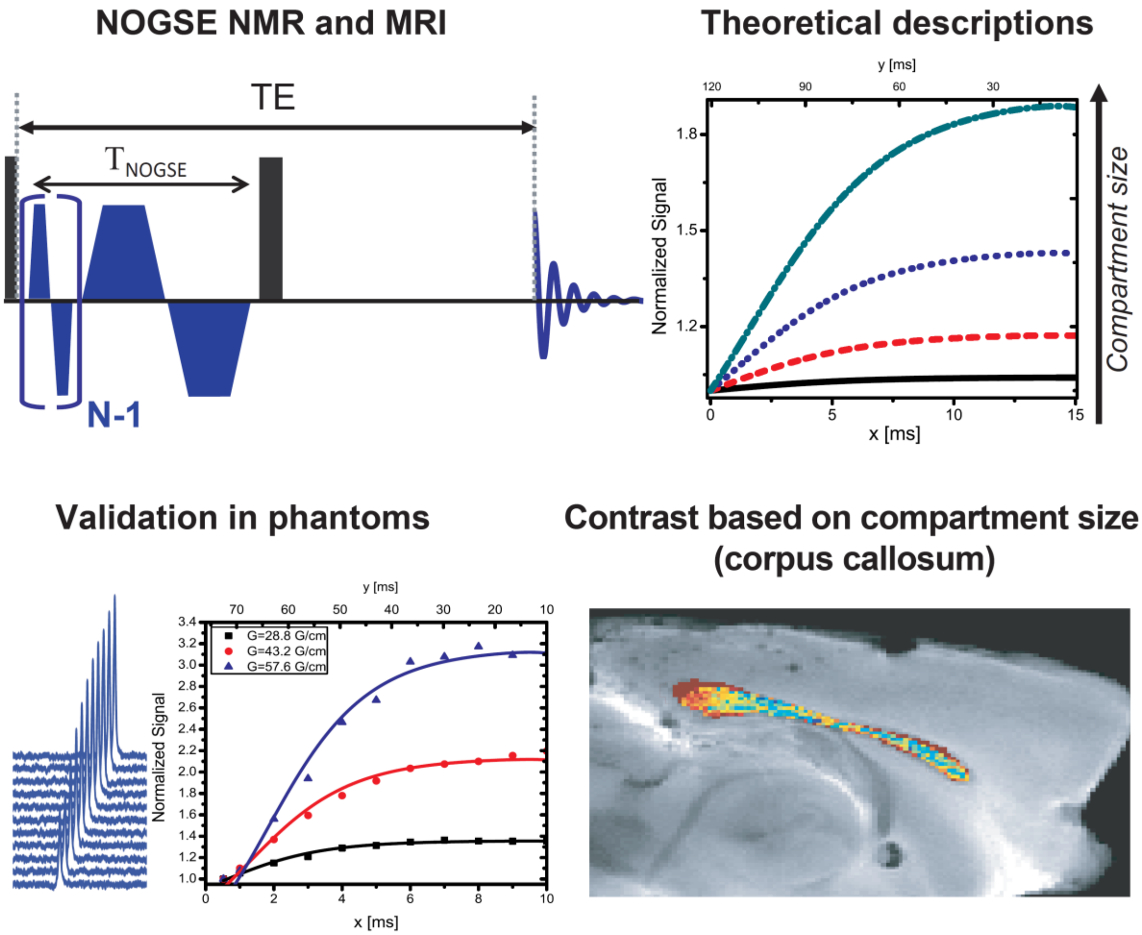

Highlights

1. NOGSE, a novel diffusion MR approach for measuring pore sizes, is presented

2. NOGSE is based on a constant time and a constant number of oscillating gradients

3. Experiments on microstructural phantoms, spinal cords and brains, validate NOGSE

Introduction

Systems comprised of fluid- or gas-filled pore networks are ubiquitous in Nature [1]; they range from rocks to biological tissues, and their microstructural topologies often determine many physicochemical and/or biological properties of the systems. When Brownian motions become restricted by such physical boundaries, NMR-based diffusion measurements can deliver a wealth of information on morphological attributes of the porous domains [2,3]. The vast majority of contemporary diffusion NMR sequences rely on the Pulsed-Gradient Spin-Echo (PGSE) NMR approach developed by Stejskal and Tanner [4], which is sensitive to the dephasing experienced by mobile spins during a diffusion time Δ separating a pair of diffusion-sensitizing gradients $\boldsymbol{G}$. The diffusion process can be characterized from the ensuing signal attenuation [3]. Since PGSE requires no external agents for extracting its diffusion information, it offers a unique opportunity to noninvasively probe structural aspects of clear or opaque systems, with capabilities that have seen extensive applications in microstructural interrogation of porous materials [5] as well as in diverse biological systems [6]. Notably, diffusion anisotropy can be detected and utilized for characterizing White Matter (WM) tracts *in-vivo* [7], and diffusion-driven compartment size estimations provide unique contrasts within WM [8].

Diffusion sensitization in PGSE MR consists of spatial labeling elements represented by the q-vector $\boldsymbol{q} = (2\pi)^{-1}\gamma\delta\boldsymbol{G}$, where δ is each gradient's duration, and of a temporal inter-gradient element given by the diffusion period Δ. In solution, where free diffusion takes place, the diffusion-driven signal attenuation will follow a Gaussian decay:

$$E(q,\Delta) = e^{-(2\pi q)^2\left(\Delta-\frac{\delta}{3}\right)D_0}, \tag{1}$$

where D_0 is the free diffusion coefficient [9]. When restricting boundaries are imposed on the system, the signal decay may significantly deviate from this relation [3]; the choice of the q-vector and Δ values can then profoundly affect the diffusion-driven NMR signal decay. In the completely restricted diffusion regime ($\Delta \rightarrow \infty$) and under the short-gradient-pulse approximation ($\delta \rightarrow 0$), the diffusion-driven signal decay will (at least in systems narrowly dispersed in size) exhibit diffusion-diffraction patterns, reflecting interferences among different phase dispersions accumulated at different q-values by the confined spins [10]. Although diffusion-diffraction patterns may yield the compartment size directly from the inverse of the q-value corresponding to the first diffraction minimum [3,10], they are rapidly lost in the presence of size polydispersity [11]. Alternatively, the restricting length scales can also be inferred by manipulating the temporal element of the diffusion weighting, Δ [12]. At low q-values for example, restriction effects are recast as time-dependent apparent diffusion coefficients (ADCs). In this regime, Eq. 1 becomes:

$$E\left(q \ll \frac{1}{2\pi l_c}, \Delta\right) = e^{-(2\pi q)^2\left(\Delta - \frac{\delta}{3}\right)ADC(\Delta)}. \tag{2}$$

For very short Δ-values $\Delta \ll l_c^2/2D_0$, where 'l_c' is the correlation length associated with the restricting length scale, the ADC will approach D_0 (up to surface to volume and tortuosity effects [13]). With increasing Δ, the ADC will diminish due to the effects of restrictions, and will plateau once the fully restricted diffusion regime has been reached. Such Δ-dependent measurements circumvent the strong gradients required for observing diffraction-patterns, yet still afford unique insights into the microstructure of tissues [14] and heterogeneous porous systems [15].

Resolving small pore sizes using either of these PGSE approaches, however, still poses significant challenges. In q-space experiments, the inverse relationship between diffraction minima and pore size demands extremely strong gradients, which are generally unavailable in animal or clinical systems. When the time-dependence of the ADC is considered, Δ cannot usually be made sufficiently short to manifest the transition from free to restricted diffusion, whose robust detection is needed for inferring compartment sizes [16]. This is further exacerbated by diffusion *during* the gradient pulse, which effectively "reduces" the apparent pore size [17]. A possible remedy for these limitations arises from replacing the PGSE block, which can be considered as a single "modulation" of the gradient waveform, with oscillating gradient waveforms [18-22]. The Oscillating-Gradient Spin-Echo (OGSE) methodology in particular utilizes constant-frequency oscillating-gradient waveforms, where the diffusion period can be approximated to be proportional to the inverse of the oscillation frequency [16,23]. The shorter time scales accessible by increasing the frequency of the gradient oscillations accentuate the transition between free and restricted diffusion regimes [20], and hence allow characterization of small compartment dimensions. Ideally OGSE will probe a single element in the diffusion-driven frequency fluctuations of the particles in question, $D(\omega)$, per each experiment [16]; requiring that the gradient frequency spectrum consists of a single frequency and be devoid of a zero component, however, imposes stringent conditions on the hardware [24]. Still, OGSE methodologies have gained increasing use in recent years, with applications to probing micro-architecture of normal [25,26] as well as diseased [27,28] tissues, as well as for enhancing contrast in diffusion tensor approaches [29]. Modulating a constant gradient with π-pulses and monitoring deviations from spectral density power laws [30,31], have also been suggested as routes for probing compartment sizes. It has been recently shown that gradient waveforms can be numerically tailored to garner sensitivity towards specific desired sizes when distributions are of interest [32-34], and that phase information on the pore structure function can be retained from more complex gradient waveforms [35-37].

In this study, we present a new approach for measuring compartment sizes noninvasively, which is also based on gradient modulations. The approach is related to OGSE in that it employs modulated gradient waveforms, but its main basis relies on dynamical decoupling concepts [38], where *non-uniform* temporal modulations are created by departing from the dogma of applying equidistant pulses. Such temporally non-uniform modulations can be used, for example, to prolong the coherence lifetimes of spins if decoherence is due to noise containing only certain frequency components – a concept which has been recently suggested as a novel source contrast in MRI [39]. Inspired by these proposals we have recently suggested the Selective-Dynamical-Recoupling (SDR) approach [40] (Figure 1A), a new class of experiments which can achieve coherent evolutions via such non-equidistant modulations. Importantly, these modulations are performed at a constant time and with a fixed number of refocusing π-pulses, rendering SDR robust towards T_2- and pulse-related sources of decoherence. SDR has been proven useful for probing chemical shift identities driven by coherent (J-couplings) or incoherent (chemical exchange) perturbations [40], and has recently been extended towards selective probing of restricted diffusion [41]. In this study, SDR's sensitivity towards small compartment dimensions is augmented by replacing the non-uniform refocusing π-pulses previously used [40,41], with non-uniform gradient modulations. The ensuing Non-uniform Oscillating-Gradient Spin-Echo (NOGSE) methodology leads to a signal response that is hereby shown to be strongly dependent on compartment size. In fact, NOGSE's NMR response bears a unique sensitivity towards the time in which the diffusion mode shifts from free to restricted, while being devoid of all other potential sources of decoherence. This paper presents a brief overview of the theory for NOGSE experiments, and validates the approach on a microstructure phantom where the ground truth is *a-priori* known. NOGSE MRI implementations then reveal apparent restricting length scales in *ex-vivo* pig spinal cord and mouse brain white matter (WM). Owing to its simplicity, and due to the relatively low gradients needed for resolving even small compartment sizes, the NOGSE methodology bodes well for compartment dimension measurements in porous systems, especially in the context of the Central Nervous System.

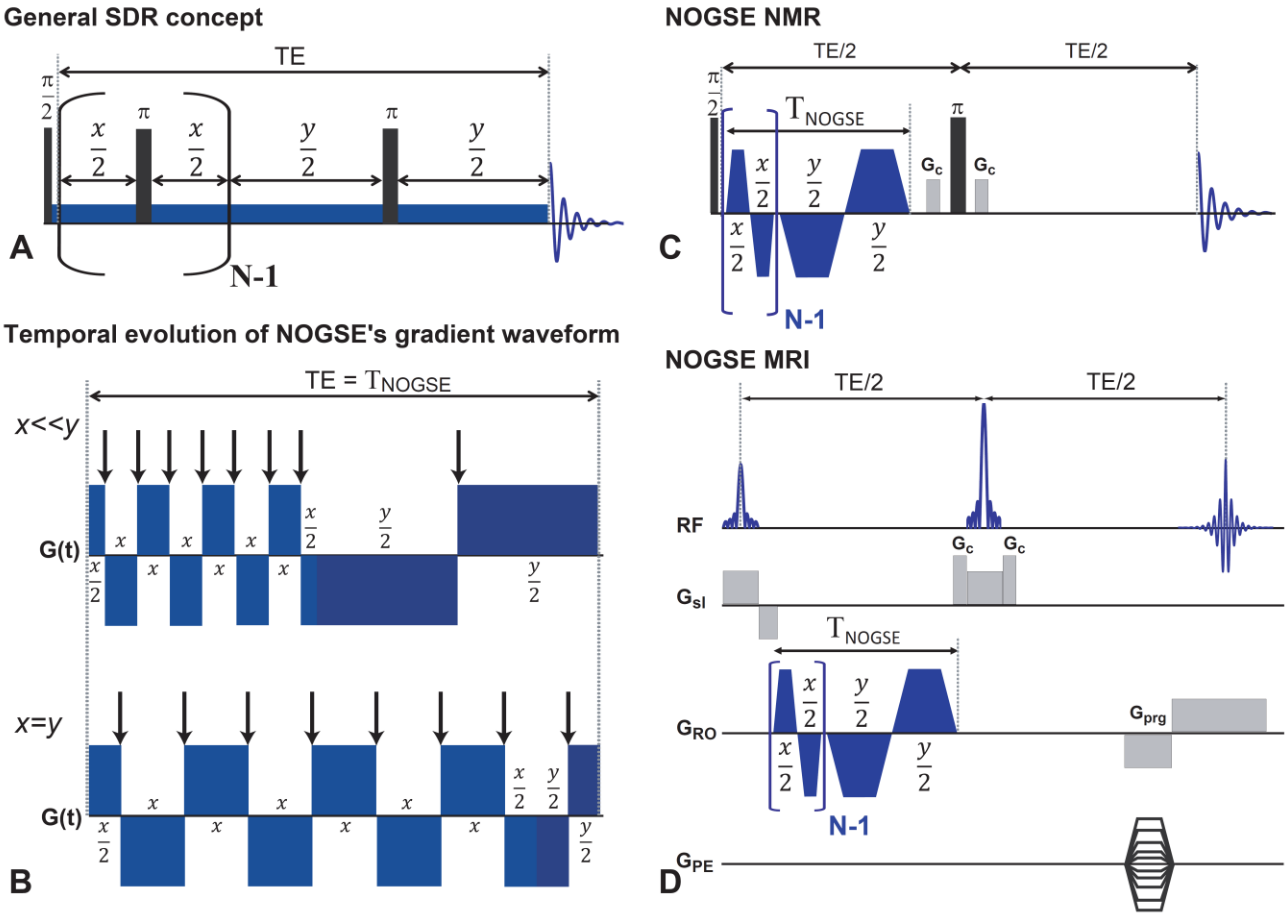

Figure 1. Concepts and sequences considered in this work. (A) The SDR approach entails an initial excitation pulse, followed by a CPMG-like block consisting of *(N-1)* refocusing pulses and concluded by a single Hahn-echo block consisting of a single refocusing pulse. For the purposes of NOGSE, it is assumed that a constant gradient exists throughout the entire echo time (*TE*). The characteristic time of the CPMG-like block is x while the characteristic time of the Hahn-like sequence is $y = TE - (N-1)x$. **(B)** Effective gradient waveforms *G(t)* arising from the SDR approach (A); the upper and lower panels show the two extremes ($x << y$ and $x = y = TE/N$) of the ensuing NOGSE waveform. Arrows indicate the timing of (the now removed) refocusing RF pulses. **(C)** NOGSE NMR sequence used in this study, replacing SDR's succession of π-pulses with an equivalent oscillating gradient waveform (shown in blue). Note that the entire diffusion-weighting period occupies only the first half of a spin echo sequence, with the new constant modulation time $x(N-1)+y$ defined as T_{NOGSE}, to distinguish it from the total echo time (*TE*) of the sequence. The x and y periods include the gradient ramps in their definitions. N is the total number of gradient polarity switches, and G_c indicates small crusher gradients. **(D)** NOGSE MRI sequence implemented in this study, using the same general concepts as in (C) but with (i) RF pulses replaced by slice-selective pulses, and (ii) phase encoding gradients (G_{PE}), readout gradients (G_{RO}) and a purge gradient (G_{prg}) added prior to and during the acquisition window. In our implementation of NOGSE, the final gradient oscillation was in opposite polarity (*e.g.*, positive then negative).

Theory

The SDR sequence on which NOGSE is based, is shown in Figure 1A. This sequence's central feature is a concatenation of a CPMG block $(x/2 - \pi - x/2)_{[N-1]}$ and a Hahn block $(y/2 - \pi - y/2)$, where x and y denote variable delays and N denotes the (constant) total number of radiofrequency

(RF) pulses. The SDR methodology entails simultaneously varying x in the range $0 \leq x \leq \frac{TE}{N}$, and y in the range $\frac{TE}{N} \leq y \leq [TE - x(N-1)]$ in a 2D-NMR-like fashion, so that the overall sequence timing stays constant at *TE*. Assuming that the SDR sequence is implemented under a constant gradient *G* aimed at monitoring diffusion-driven decoherence processes, effective gradient waveforms *G(t)* are thus created; two of these are shown in Fig. 1B. The upper panel of the figure illustrates the initial implementation of the SDR sequence, corresponding to $x<<y$; the waveform for the final SDR point, $x=y$, is shown in Fig. 1B's lower panel. Such waveforms are generated in NOGSE by gradient switching rather than by refocusing π-pulses. Relying on such gradient modulations rather than on non-equidistant refocusing pulses is especially valuable for avoiding unwanted excitation profiles or complications in coherence pathway selections arising from multiple (and in some cases imperfect) pulses.

To compute the NOGSE NMR signal in the context of diffusion in restricting environments, we assume the Gaussian Phase Distribution approximation for the spin's random displacements [42]. The diffusion-weighted echo signal in presence of oscillating gradients can then be described as [18]:

$$E(TE) = \exp\{-\beta(TE)\} = \exp\left\{-\frac{\gamma^2}{2}\int_0^{TE} dt_1 \int_0^{TE} dt_2\, G(t_1)\langle r(t_1)r(t_2)\rangle G(t_2)\right\}, \qquad (3)$$

where $\beta(TE)$ is a signal attenuation factor at the echo time, *G(t)* depicts the gradient value at a specific time, $r(t)$ is the projection of the spins' position along the axis in which the gradient is applied at time t, and the brackets <> denote an ensemble average. Eq. 3 can be recast in a Fourier transform representation where $\beta(TE)$ is then given by [30,31,41]:

$$\beta(TE) = \frac{\gamma^2}{2\pi}\int_{-\infty}^{\infty} |F(\omega, TE)|^2 S(\omega). \qquad (4)$$

$S(\omega)$ is the displacement power spectrum given by the FT of the displacement correlation function $g(\tau) = \langle r(0)r(\tau)\rangle$ [30,31] and $F(\omega, TE)$ is a filter function given by the FT of the gradient modulation $\boldsymbol{G}(t)$. The displacement power spectrum $S(\omega)$ is related to OGSE's diffusion spectrum $D(\omega)$ [16], by the expression $D(\omega) = \omega^2 S(\omega)$ [30,31]. For well-defined pore geometries, the displacement power spectrum $S(\omega)$ is a sum of Lorentzian functions with different weights and correlations times [31,43]. Usually, only one of these Lorentzians is significant, and at least for planar, spherical and cylindrical constraining geometries, this dominant first term will dominate the NOGSE evolution [41]. Considering only this dominant term, the spectrum $S(\omega)$ will then be given by

$$S(\omega) = \frac{D_0 \tau_c^2}{(1 + \omega^2 \tau_c^2)\pi}. \tag{5}$$

τ_c is the correlation time associated with the diffusion process, and is related to the correlation length scale, l_c, by the Einstein expression:

$$l_c^2 = 2D_0 \tau_c, \tag{6}$$

where D_0 is the free diffusion coefficient. Note that τ_c is effectively the time required for most of the molecules to fully probe the pore boundaries. The specific relation between l_c and the restriction length of the pore will depend on its geometry; for cylinders a good approximation is $\tau_c = 0.262 d^2 / D_0$, where d is the cylinder diameter [31,43], and then $l_c \approx 0.37d$.

The spin-echo sequence of Fig. 1A generates an effective array of modulating gradient $G_{N,x,y}^{NOGSE}(t)$; two components of these gradient waveforms are shown in Fig. 1B for the $x << y$ and $x = y$ extremes. In general, these gradient waveforms' temporal modulations can be described as

$$G_{N,x,y}^{NOGSE}(t) = G_{N-1}^{CPMG}(t, (N-1)x) + (-1)^{N-1} G_1^{Hahn}(t - (N-1)x, y), \tag{7}$$

where G_{N-1}^{CPMG} and G_1^{Hahn} are CPMG- and Hahn-modulating functions, respectively. The filter function $\left|F_{N,x,y}^{NOGSE}(\omega, TE)\right|^2$ associated with NOGSE will therefore have multiple peaks, at discrete frequencies [41,44,45]. On the basis of Eq. 7, this filter can be described by the sum of a CPMG filter, a Hahn filter, plus a cross term representing an interference between the two:

$$\begin{aligned}\left|F_{N,x,y}^{NOGSE}(\omega,TE)\right|^2 &\propto \left[FT\left\{G_{N,x,y}^{NOGSE}(t)\right\}\right]^2 \\ &= \left|F_{N-1}^{CPMG}(\omega,(N-1)x)\right|^2 + \left|F_1^{Hahn}(\omega,y)\right|^2 \\ &+ (-1)^{N-1}2\mathrm{Re}\left\{e^{i\omega[TE-y]}F_{N-1}^{CPMG}(\omega,(N-1)x)\,\overline{F_1^{Hahn}(\omega,y)}\right\}.\end{aligned} \tag{8}$$

This filter-function formalism allows one to derive a solution for the resulting signal decay given by:

$$\begin{aligned}&M_{NOGSE}(TE,x,y,N) \\ &\quad= M_{CPMG}\big((N-1)x,N-1\big)\times M_{Hahn}(y) \\ &\quad\times M_{Cross-NOGSE}(TE,x,y,N).\end{aligned} \tag{9}$$

Full analytical expressions for M_{NOGSE} and its constituents can be derived along the lines of the description given in Ref. [41], and they are given in full in the Appendix.

The general theory presented above is described for the entire gradient modulation period, T_{NOGSE}, which, in Figures 1A and 1B, coincides with *TE*. In the NOGSE NMR and NOGSE MRI sequences (Figures 1C and 1D), the expressions above describe the magnetization evolution during T_{NOGSE}, and it is assumed that any further contributions outside of this time interval can be factored out. Therefore, we will just focus on the behavior of the magnetization decay during T_{NOGSE} in the limiting values $x = 0$ and $x = T_{NOGSE}/N$. For $x \sim 0$, $M_{NOGSE}(T_{NOGSE}, x \sim 0, y, N) = M_{Hahn}(y)$ while for $x = y = T_{NOGSE}/N$, $M_{NOGSE}(T_{NOGSE}, x = y = T_{NOGSE}/N, N) = M_{CPMG}(T_{NOGSE}, N)$. Therefore NOGSE's maximum amplitude modulation, ΔM_{NOGSE}, is contrasting the difference between a CPMG and a Hahn modulation: $\Delta M_{NOGSE} = M_{CPMG}(T_{NOGSE}, N) - M_{Hahn}(y)$. In particular, if $x << \tau_c << y$, the decay of the signal is dominated by the Hahn portion of the sequence and the attenuation factor approaches $\beta_{Hahn}^{restricted}(T_{NOGSE}) = \gamma^2 G^2 D_0 \tau_c^2 (T_{NOGSE} - 3\tau_c)$; by contrast, if $x = y = \frac{T_{NOGSE}}{N} >> \tau_c$, the NOGSE attenuation factor will be $\beta_{CPMG}^{restricted}(T_{NOGSE}, N) = \gamma^2 G^2 D_0 \tau_c^2 (T_{NOGSE} - (2N+1)\tau_c)$.

Note that the first terms at both extremes of the NOGSE sequence appear identical, and yield an exponential signal decay. By contrast, the second terms are independent of T_{NOGSE} and are consequently constant. The difference between these two attenuation factors, $\varDelta\beta_{NOGSE}^{restricted}(T_{NOGSE}, N) = -2(N-1)\gamma^2 G^2 D_0 \tau_c^3$, will thus be manifested as an amplitude modulation, $\varDelta M_{NOGSE}$ (see Figure 2). This modulation probes τ_c – and hence the confinement length l_c – as an exponential factor that is proportional to $(N-1)\tau_c^3 \propto (N-1)l_c^6$. This contrasts with the exponential rates typically used for determining l_c in conventional OGSE sequences, which derive from the first term of the attenuation factor, and are thus proportional to $\tau_c^2 \propto l_c^4$. That NOGSE's sensitivity to compartment size amplifies with the sixth power of l_c and with *N*, suggests that the defining restricting length scale could be probed by less demanding gradient amplitudes. This central feature is illustrated below. This central feature is illustrated below. Finally, if free, unobstructed diffusion is considered ($x,y<<\tau_c$), it is straightforward to show that $\beta_{NOGSE}^{free}(T_{NOGSE}, N, x, y) = \frac{1}{12}\gamma^2 G^2 D_0\{(N-1)x^3 + y^3\}$ and then the difference between the two extremes $x=0$ and $x=T_{NOGSE}/N$ will be $\varDelta\beta_{NOGSE}^{free}(T_{NOGSE}, N) = \frac{1}{12}\gamma^2 G^2 D_0\, T_{NOGSE}^3 \left(\frac{1-N^2}{N^2}\right)$.

Materials and Methods

Simulations. Simulations for the NOGSE signal were based on Eq. 9 (for the full expression for cylinders see the Appendix), and performed using home-written code in Matlab® (Mathworks, Natick, MA, USA). All simulated signals are shown normalized to the initial $(x = Min(x))$ value of the NOGSE curve. Unless otherwise stated, $M_{NOGSE}(T_{NOGSE} = 0)$ (Eq. 9) was set to 1. See figure captions for specific details on simulated parameters.

Specimen preparation. The accuracy of NOGSE was tested on a phantom comprised of an ensemble of water-filled microcapillaries (Polymicro Technologies, Phoenix, AZ, USA) characterized by an inner-diameter of 5±1 μm. The microcapillaries were cut to ~5 cm segments, and placed in a water-filled cuvette for ca. two weeks prior to NMR experiments. The microcapillaries were then dried externally and packed into a 4 mm NMR tube opened on both sides, which in turn was inserted into a 5 mm NMR tube for placing in the magnet.

Ex-vivo specimens were also subject to NOGSE measurements. These involved formalin-fixed pig spinal cords (The Institute of Animal Research, Lahav, Israel) placed in PBS overnight prior to commencing experiments. These spinal cords were stripped from the perineural sheath, inserted into a 10 mm NMR tube filled with Fluorinert®, and given ~2 hrs to thermally equilibrate in the magnet prior to the MRI experiments. These spinal cords were aligned with their principal axis along the *z*-direction of the laboratory frame. A second set of tests involved formaline-fixed mouse brains, obtained from healthy adult mice. These brains were immersed in 4% PFA for several days, then washed twice with PBS and left overnight immersed in PBS. The mouse specimen was then placed in a 10 mm NMR tube filled with Fluorinert. Care was taken to align the anterior-posterior axis of the brain with cylindrical axis of the NMR tube, coinciding with the B_0 direction.

NOGSE NMR and MRI experiments. All experiments were performed on a vertical bore Bruker Avance system operating at 9.4 T (400.17 MHz for ^{1}H) equipped with a Micro5 imaging probe and gradient coils capable of generating 291 G/cm. Unless otherwise stated, all experiments in this study were performed in the direction of restriction; *i.e.*, with the gradients oriented along the transverse, most restricted specimen dimension. All NOGSE experiments were performed using a gradient ramp time of 80 μs. The NOGSE NMR experiments were conducted using the sequence shown in Figure 1C.

NOGSE MRI experiments were performed using the sequence shown in Figure 1D. Spinal cord were imaged with the following imaging parameters: isotropic Field of View (FOV)

= (9 mm)^2, slice thickness = 3 mm, 64x64 matrix size leading to an in-plane resolution of ~140 x 140 (μm)^2, TR / TE = 4000 / 51 ms, two dummy scans, and two averages. The receiver bandwidth was 50 kHz. The experiment time for each point in the NOGSE curve was ~ 9 minutes.

PGSE experiments were also conducted on spinal cords by replacing the NOGSE block in Figure 1D with a simple PGSE block consisting of a single pair of bipolar gradients $(+\boldsymbol{G} - (\Delta\text{-}\delta) - \text{-}\boldsymbol{G})$, where the gradients' duration were δ and the gradient separation was Δ. The PGSE experiment was conducted with identical imaging and timing parameters as the NOGSE MRI experiments.

NOGSE experiments on the mouse brain were performed using the following imaging parameters: FOV = 12.8 x 8.6 mm^2, slice thickness = 550 μm, matrix size = 212x144 (where the larger matrix element was carried out in the readout direction) leading to an in-plane resolution of ~60 x 60 (μm)^2, TR / TE = 3500 / 53 ms, two dummy scans, and 12 averages. The receiver bandwidth was 50 kHz. The experiment time for each point in the NOGSE curve was ~ 1.6 h. A T_2 weighted image was further obtained from a NOGSE experiment with G=0 G/cm.

Data fitting and the extraction of compartment sizes. Data from NOGSE NMR experiments on microcapillaries were fitted to Eq. 9 leading to correlation times τ_c along with their respective errors. D_0=2*10^{-5} cm^2/sec was set from a PGSE measurement along the z-axis (the principal axis of the microcapillaries), and the correlation length scale l_c was then obtained from the Einstein relation (Eq. 6). As the cylindrical shape of the microcapillaries was known, the compartment diameter was obtained from $d = l_c/0.37$ [31,43], and the error was propagated from the correlation time to the diameter.

Spinal cord and mouse brain NOGSE MRI data were analyzed as the microcapillaries data. When ROIs are presented, the signal represents the mean value for the pixels within the

ROI. The NOGSE-derived compartment size maps shown in Figures 6-8 were obtained from a pixel-by-pixel fit of the data to Eq. 9. For both of these biological systems, D_0 was chosen to be 0.7*10^{-5} cm^2/sec, in agreement with previous literature [27,46], and in accordance with our experimental tests. All experimental fits assume that NOGSE oscillations are rectangular; no significant errors are expected from this assumption [23].

Compartment size maps obtained from conventional PGSE measurement in the spinal cord (Figure 6D) were derived from a pixel-by-pixel fit of the signal to Eq. 2 to obtain the ADC, then the compartment diameter was obtained (assuming cylindrical compartments) from $d = \sqrt{(2 * ADC * \mathit{\Delta})}/0.37$.

Results

Simulations depicting the general characteristics of the NOGSE signal for different diffusion scenarios are presented in Figure 2. Figure 2A shows the general hallmarks of the NOGSE signal in restricted systems: in the short time regime $x << y$, when the x-delay (here given in x/τ_c dimensionless units in the lower abscissa) is increased, the NOGSE signal increases, and as x is increased such that it exceeds ~5τ_c, the signal approaches an asymptote. This behavior reflects the fact that at short x/τ_c a majority of spins does not experience restriction during the first OGSE-like part of the pulse sequence and are filtered; the signal that survived the oscillating filter then experiences the effects of restricted diffusion. The NOGSE signal in this $x \ll y$ regime is therefore given by $M_{NOGSE}(T_{NOGSE}, x \sim 0, y, N) \sim M_{Hahn}(y)$. As x increases, the y-argument of M_{Hahn} becomes correspondingly shorter, which in turn results in a net signal increase. Yet at the same time, spins begin to experience the effects of restriction also during the CPMG-like modulation of NOGSE, *i.e.*, also during the x-periods. For $x/\tau_c \geq 5$, most of the pore has been probed, and the signal reaches the effective plateau (Figure 2A, note that the lower abscissa, plotted in dimensionless units, corresponds to the parameters given in the lower right legend, whereas the upper abscissa, which is plotted in units of time, corresponds to the parameters given in the upper left legend). Importantly, this characteristic behavior mirrors the temporal dynamics of the transition between the free and the restricted diffusion regimes. Figure 2B presents the same curves, only with the signal now plotted against y/τ_c in the lower abscissa. The restricted diffusion signal's plateau is in the initial part (left-hand side) of the curve corresponding to the long x/τ_c regime; the subsequent decrease in signal with increasing y/τ_c reflects the Hahn-like decay dominance $M_{NOGSE}(T_{NOGSE}, x \sim 0, y, N) \sim M_{Hahn}(y)$ with decreasing x, as mentioned above.

Figures 2C and 2D illustrate the NOGSE signal dependence on the total number of gradient oscillations N for a cellular-like compartment size l_c=2 μm. Increasing N yields increasing contrast between the free and restricted diffusion regimes, as manifested by the larger differences between the initial and final points of the NOGSE curves. This is as discussed in the "Theory" section. Note that the attenuation plots converge near $x=0$ (Figure 2C): in this limit, the first oscillation amounts to zero diffusion weighting regardless of N, and the NOGSE signal is solely weighted by the Hahn-like decay – which, reflects completely restricted diffusion behavior and filters signals by identical weightings irrespective of N. Also noteworthy is the convergence of the plots to an identical linear relationship at very long y – a consequence of $M_{NOGSE}(T_{NOGSE}, x \sim 0, y, N) = M_{Hahn}(y)$, which is again independent of N.

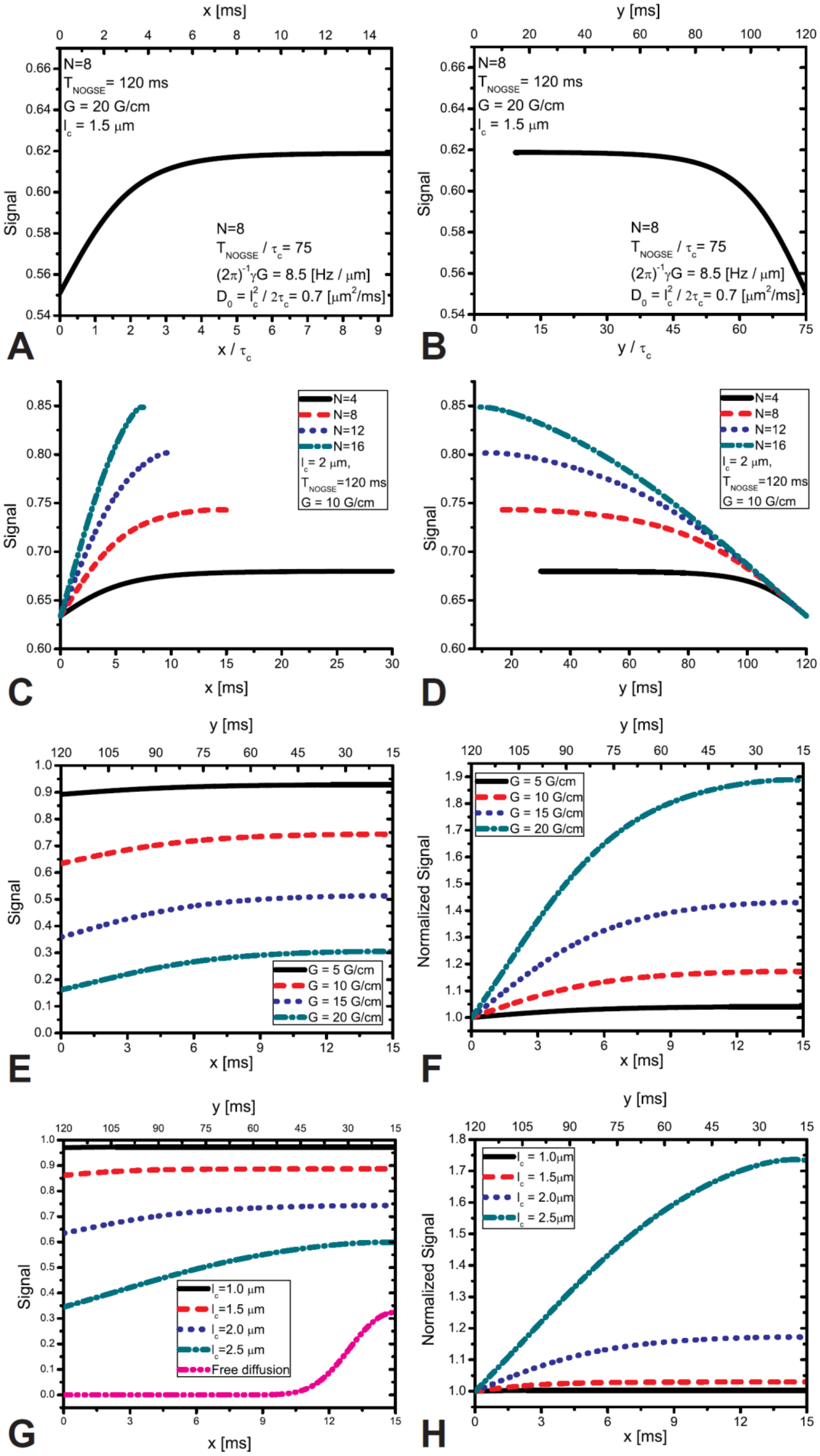
A
x [ms]
x / τ_c
Signal
N=8
T_{NOGSE} = 120 ms
G = 20 G/cm
l_c = 1.5 μm
N=8
T_{NOGSE} / τ_c = 75
$(2\pi)^{-1}\gamma G$ = 8.5 [Hz / μm]
$D_0 = l_c^2 / 2\tau_c$ = 0.7 [μm²/ms]
0.54
0.56
0.58
0.60
0.62
0.64
0.66
0
2
4
6
8
10
12
14
0
1
2
3
4
5
6
7
8
9
B
y [ms]
y / τ_c
Signal
N=8
T_{NOGSE} = 120 ms
G = 20 G/cm
l_c = 1.5 μm
N=8
T_{NOGSE} / τ_c = 75
$(2\pi)^{-1}\gamma G$ = 8.5 [Hz / μm]
$D_0 = l_c^2 / 2\tau_c$ = 0.7 [μm²/ms]
0
20
40
60
80
100
120
0
15
30
45
60
75
C
Signal
x [ms]
N=4
N=8
N=12
N=16
l_c = 2 μm,
T_{NOGSE}=120 ms
G = 10 G/cm
0.60
0.65
0.70
0.75
0.80
0.85
0
5
10
15
20
25
30
D
Signal
y [ms]
N=4
N=8
N=12
N=16
l_c = 2 μm,
T_{NOGSE}=120 ms
G = 10 G/cm
20
40
60
80
100
120
E
y [ms]
x [ms]
Signal
G = 5 G/cm
G = 10 G/cm
G = 15 G/cm
G = 20 G/cm
120
105
90
75
60
45
30
15
0
3
6
9
12
15
0.0
0.1
0.2
0.3
0.4
0.5
0.6
0.7
0.8
0.9
1.0
F
y [ms]
x [ms]
Normalized Signal
G = 5 G/cm
G = 10 G/cm
G = 15 G/cm
G = 20 G/cm
1.0
1.1
1.2
1.3
1.4
1.5
1.6
1.7
1.8
1.9
G
y [ms]
x [ms]
Signal
l_c=1.0 μm
l_c=1.5 μm
l_c=2.0 μm
l_c=2.5 μm
Free diffusion
H
y [ms]
x [ms]
Normalized Signal
l_c = 1.0μm
l_c = 1.5μm
l_c = 2.0μm
l_c = 2.5μm
1.0
1.1
1.2
1.3
1.4
1.5
1.6
1.7
1.8

Figure 2. NOGSE signal simulations for different experimental parameters. (A-B) NOGSE signal as function of x and y, plotted in dimensionless units (lower abscissa and lower legend) and in units of time (upper abscissa and upper legend). Note in (A) the characteristic NOGSE signal increase followed by a plateauing once the fully restricted diffusion regime is achieved. This amplitude modulation, ΔM_{NOGSE}, is proportional to l_c^6 and can characterize the restricting length scale with good sensitivity. **(C-D)** NOGSE signal as function of x and y, respectively, plotted for different number of oscillations, N. Note that as N increases, the maximum x obtained at the same T_{NOGSE} is reduced to T_{NOGSE}/N. Also apparent is the increase in NOGSE contrast for increasing N, although it should be noticed that as the plateau effect is reduced, the restricted diffusion regime is not fully met. Note as well the convergence of the plots at x=0 and at long y-values, reflecting the diminished influence of the CPMG-like part of the oscillations when x approaches zero. For both (A) and (B), l_c=1.5 μm and G=20 G/cm. **(E-F)** Dependence of NOGSE's signal on the gradient amplitude for l_c=2 μm and N=8. (E) plots the absolute signal, and (F) plots the normalized signal after each curve was normalized to its initial point. It follows that although with increasing G the signal begins from a lower absolute value, the dynamic range (and the sensitivity) of the experiment increases. **(G-H)** Dependence of NOGSE signal on the compartment size, l_c, plotted in conventional scale (G) and in a scale normalized to the first point of each curve (H) for G = 10 G/cm and N=8. Notice how the contrast varies strongly with just small increases in monodisperse compartment size. Note, that when free diffusion (infinite l_c) is considered does not exhibit any plateau characteristics. The free diffusion curve is not shown in (H) since effectively, at short x, M_{NOGSE} will be very small for the above-mentioned parameters, hence the normalized curve will appear out of scale. For all simulations, T_{NOGSE}=120 ms and D_0 = 0.7*10^{-5} cm^2/sec.

Figures 2E and 2F show the NOGSE signal attenuation as function of x and y for different gradient amplitudes. As gradient amplitudes increase, the signal begins at lower initial values, due to the increased sensitivity towards free diffusion effects in the $x/\tau_c \ll 1$ regime (Fig. 2E). The signal increases with increasing x as described above for all gradient amplitudes. Notice that while the overall NOGSE signal decreases with the gradient strength (Fig. 2E), the NOGSE amplitude *contrast*, ΔM_{NOGSE}, actually increases when the gradients are increased. The magnitude of these changes for different gradients is better viewed in a normalized scale, where each curve is scaled by its first (Min(x)) point (Fig. 2F). A strong increase in NOGSE contrast, $\propto G^2$, is then evident with increasing gradients. This reflects the fact that although the transition between the free and restricted diffusion regimes occurs at the same x for all gradient amplitudes, the frequency fluctuation per unit of displacement increases with increasing gradient amplitude. The sensitivity of the NOGSE signal towards the freely diffusing spins, as well as NOGSEs contrast vis-à-vis compartment size, thereby grows with gradient strength.

Figure 2G shows NOGSE curves for varying restricting length scales but for constant NOGSE parameters. Examination of these plots demonstrates NOGSE's signal attenuates with increasing restriction length, a result of an increasing fraction of freely diffusing molecules in a given pore at shorter x-values. Also plotted in this panel is the NOGSE signal for free diffusion; note, that by contrast with restricted diffusion, there are no plateau characteristics since the correlation length is infinite for free diffusion. The normalized plots shown in Figure 2H depict the ensuing high sensitivity of NOGSE contrast towards compartment sizes: whereas a 1 μm compartment gives rise to ~5% amplitude modulation between the first and last NOGSE points, a 2 μm compartment size bears a ~70% signal change between the first and last point of the curve. Such sensitivity to small restricting length scales even at low gradient amplitudes is a key feature of NOGSE experiments, and reflects the unique dependence of $\Delta M_{NOGSE}(T_{NOGSE}, N)$ on $(N-1)l_c^6$.

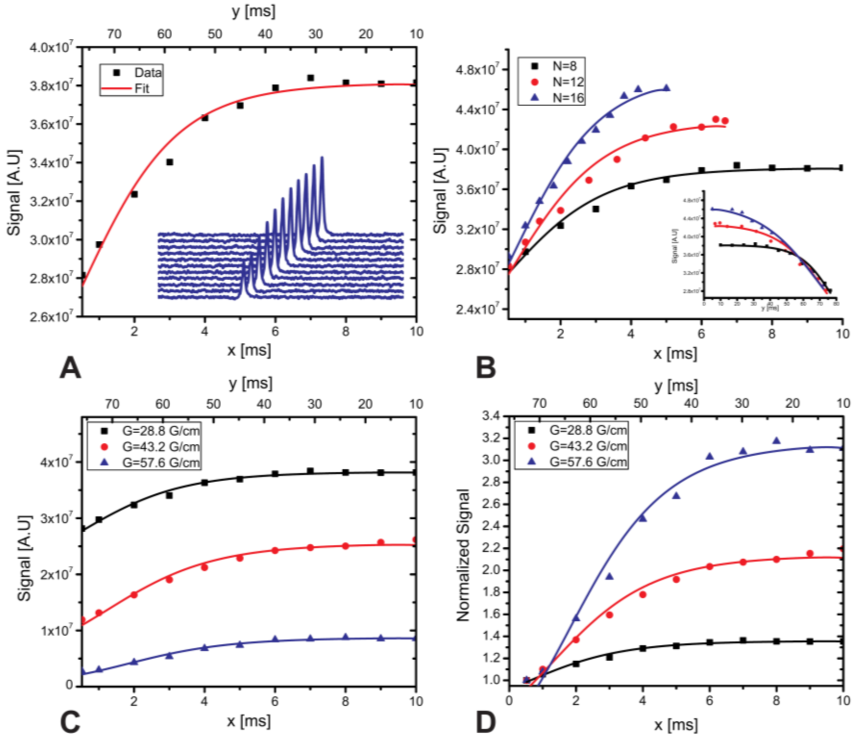

Figure 3. NOGSE NMR in a phantom system. (A) Experimental data (symbols) from a microcapillaries specimen of nominal inner diameter of 5±1 μm. The inset shows the stacked plot of a representative experiment, demonstrating the increase and plateauing of NOGSE signal with increasing *x*. Fits of these data to Eq. 9 (solid line) lead to a compartment size of 5.87±0.04 μm, in excellent agreement with the nominal inner diameter. Parameters for this experiment were *G*=28.8 G/cm and *N*=8. **(B)** Experimental dependence of the NOGSE NMR signal on *N* at *G*=28.8 G/cm. Once again, the experimental data (symbols) are in excellent agreement with the fitted curves (solid lines), and the sizes extracted from these curves was in good agreement with the nominal inner diameter (see text for details). The inset shows the data plotted as a function of *y*, demonstrating the convergence of the signal anticipated by Figure 2D. **(C-D)** Experimental dependence of the NOGSE signal on the gradient amplitude for *N*=8. In (C) absolute signal values are plotted, while in

(D) normalized signals are plotted. Note that the signal begins from a lower initial value, as predicted in Figure 2F; when the normalized signal is plotted, the G-driven contrast is enhanced. All experimental points (symbols) fitted well with the theoretical expression (solid lines), and the sizes that were obtained for all curves were in good agreement with the nominal inner diameter. All experiments were performed using the sequence shown in Figure 1C, with T_{NOGSE}=80 ms, TE=162 ms and TR = 4500 ms; the 90° and 180° RF pulse durations were 14.5 and 29 μs, respectively, and the receiver bandwidth was 4 kHz.

To validate these theoretical predictions, NOGSE NMR experiments were performed on coherently aligned, monodisperse microcapillaries filled with water. This system, in which the ground truth is known *a-priori*, has been extensively studied in previous diffusion MR methods validation studies [37,47]. Figure 3A shows a set of NOGSE NMR experiments (sequence in Fig. 1C) performed on such a phantom. Symbols represent experimental data, while the solid curve represents a regression of the data onto Eq. 9. The agreement between theory and experiments is clearly evident from this plot and a fit of the data leads to a compartment size of 5.87±0.04 μm, in excellent agreement with the nominal inner diameter provided by the manufacturer (5±1 μm). Figure 3B shows further experiments designed to test the validity of the predictions derived from Eq. 9 and shown in Figs. 2C and 2D, with respect to the number of oscillations. As N increases at fixed T_{NOGSE}, the signal evidences the predicted enhancement trends: the sizes extracted for these three experiments were 5.87±0.04, 5.75±0.04 and 5.61±0.03 μm for N=8, 12 and 16, respectively; again, all in excellent agreement with the nominal inner diameter. Figure 3B's inset offers also a different view of these experimental data, showing their plots against y-values. The NOGSE signals then clearly converge, as predicted in Figure 2D, towards a common absolute intensity $M_{NOGSE}(T_{NOGSE}, x \sim 0, y, N) = M_{Hahn}(y)$. Figures 3C and 3D show NOGSE NMR experiments for increasing gradient strengths. With increasing gradients, the overall NOGSE signal begins at lower absolute initial values but then evidences a higher sensitivity towards compartment size – all consistent with the simulations shown in Figure 2. Importantly, the compartment sizes extracted from these curves (solid lines in Figures 3C and 3D) were 5.87±0.04, 6.02±0.04, and 5.94±0.05 for G=28.8, 43.2 and 57.6 G/cm, respectively; again in very good agreement with the nominal inner diameter of 5±1 μm. We further note that experiments performed on freely diffusing water molecules closely followed the behavior predicted by the simulations shown in Figure 2G (data not shown).

Encouraged by these validations, the NOGSE MRI sequence shown in Figure 1D was applied to examine a pig spinal cord, chosen in light of its WM compartment size spatial variation [8,48]. On plotting the raw NOGSE MRI data in a common colormap scale as a function of increasing x (Figure 4A), the expected NOGSE signal increase can be readily appreciated. In grey matter (GM) regions, where water is confined to larger spaces, the NOGSE signal exhibits even greater signal increases compared to WM with increasing x. To test whether the signals follow the expected NOGSE dependence, 6 ROIs were chosen in various WM locations (see Figure 4B for ROI definitions). Figure 4C shows the x-dependence extracted from these ROIs. The NOGSE signals clearly follows the trends adumbrated in Figure 2, with increasing intensities as x is prolonged, and an eventual plateauing for some of the ROIs. Fitting these ROIs' NOGSE signals to Eq. 9 (solid lines in Figure 4C) affords compartment sizes of 7.20±0.05, 6.62±0.05, 6.40±0.05, 7.59±0.09, 7.00±0.05 and 7.00±0.11 μm for ROIs 1-6, respectively; notice the excellent agreement of these fitted curves with the experimental data. The confining sizes that are obtained at this gradient amplitude are relatively large, most likely reflecting a preferential bias towards larger pores in a size distribution, or reflecting contributions from diffusion in various tissue compartments. Figure 4D presents experiments with stronger gradients which, as explained above, should sensitize NOGSE towards even smaller compartments. NOGSE's signal contrast indeed increases with increasing x-values for this gradient (~250-450%), and is larger compared to the contrast observed with the weaker gradient (~150-200%). The sizes extracted for ROIs 1-6 from Fig. 4D are now 5.83±0.07, 5.46±0.06, 5.40±0.05, 6.25±0.05, 5.74±0.03 and 5.75±0.08 μm, respectively. These numbers are consistently smaller than those obtained using the weaker gradient; as explained earlier, this can be attributed to an increased sensitivity of the NOGSE contrast towards different elements of the pore size distribution upon increasing the gradient amplitude. We note in passing that the approximation for cylinders (*i.e.*, $d \sim l_c/0.37$) was utilized for the analysis of the entire spinal cord.

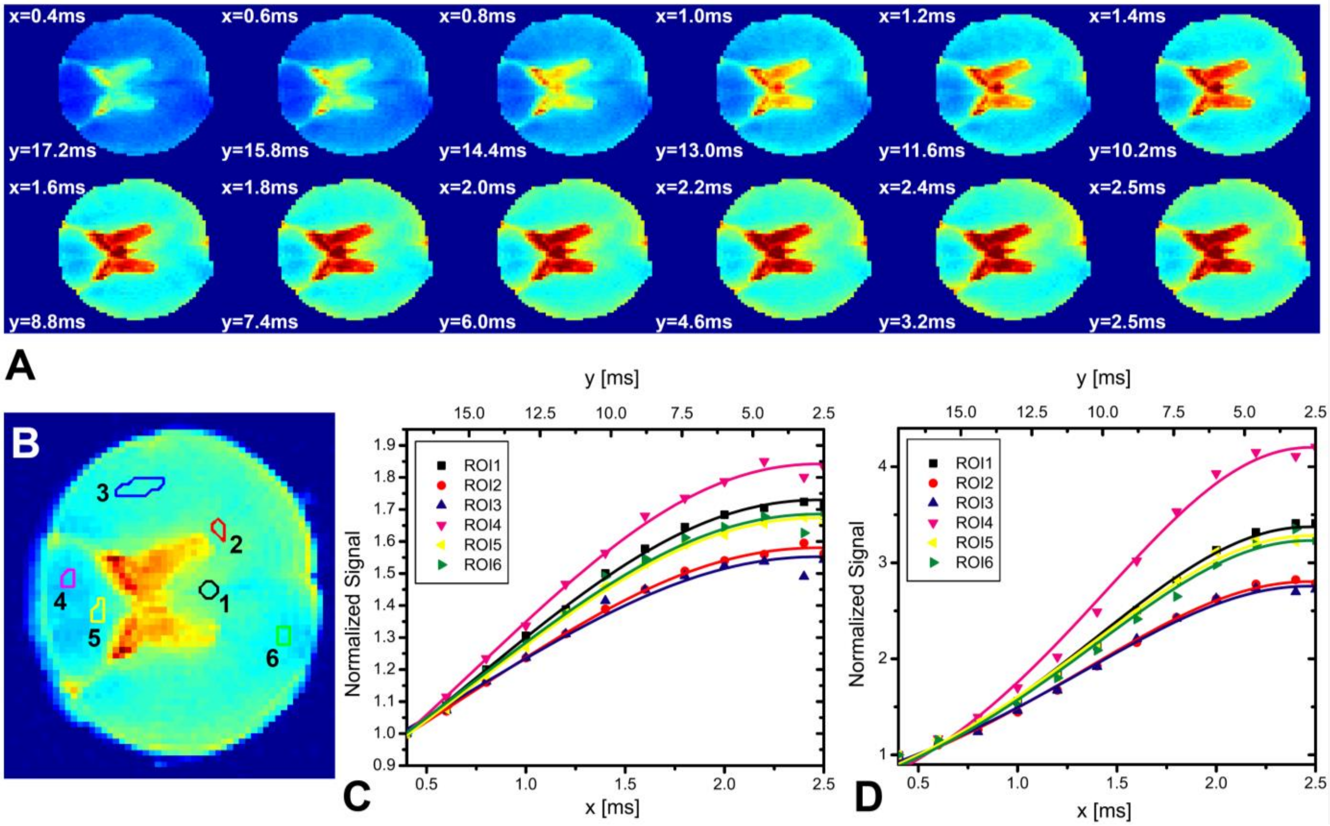

Figure 4. Ex-vivo NOGSE MRI experiments in a pig spinal cord. (A) Raw NOGSE-weighted MR images presented at a common colormap scale, with G=28.8 G/cm, N=8 and T_{NOGSE} = 20 ms. Note the clear increase in signal intensity with increasing x. **(B)** ROI definitions: all of them are placed within WM. **(C-D)** NOGSE signal modulation extracted from the indicated ROIs for G=28.8 and G=57.6 G/cm, respectively. Note the different scale bars on (C) and (D), showing ~70% signal differences in the former and >250% difference in the latter. The different ROIs' evolutions reflect different compartment sizes; fittings to the data (solid lines) are described in the text. All NOGSE MRI experiments were acquired with 12 x-values spaced between 0.4 and 2.5 ms, and the diffusion sensitizing gradients were applied perpendicular to the spinal cord's main axis.

Figures 5A-C show 2D NOGSE MRI maps based on compartment size contrast derived from a pixel-by-pixel fit to Eq. 9. The maps reveal strong contrast between gray and white matter, with larger compartment sizes detected in the GM, as expected. Of further interest is the contrast observed within the spinal cord’s WM, where different regions are delineated by the NOGSE approach. Figure 5A shows the compartment size map for G=28.8 G/cm, while Figures 5B and 5C show the compartment sizes extracted from the G=57.6 G/cm experiments. Figure 5B is presented in the same scale as Figure 5A, demonstrating that the sizes extracted at different gradient amplitudes are different. This is not predicted from the theoretical model for a monodisperse system like the capillaries in the experiments of Fig. 3; as mentioned, it is likely that such effects arise from compartment size polydispersity in the spinal cord system. Figure 5C presents the compartment size map obtained from the G=57.6 G/cm data in a different (smaller) scale; a comparison against Figures 5A reveals similar qualitative spatial patterns. Finally, although a thorough comparison of NOGSE with other noninvasive means for obtaining compartment sizes is beyond the scope of the present work, we performed conventional PGSE experiments for a qualitative comparison and to validate the overall performance of our method. Figure 5D shows a map of the compartment sizes obtained for the same slice upon fitting the ADCs obtained from a conventional PGSE experiment to the Einstein equation (Eq. 6). Note that while resembling the NOGSE map, this PGSE-derived compartment size map shows less variation between the different WM regions – reflecting the lower sensitivity of PGSE towards small compartment sizes.

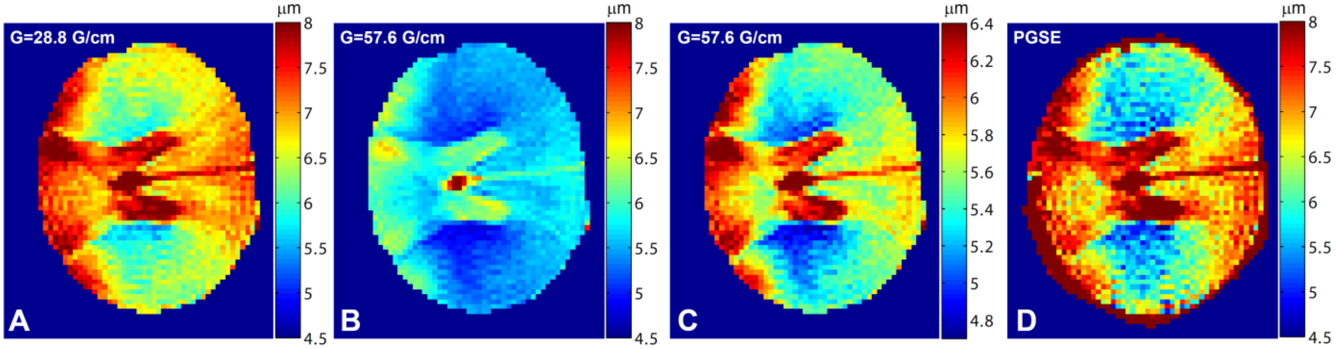

Figure 5. Compartment dimension maps for an ex-vivo spinal cord section obtained from NOGSE and PGSE MRI with different gradient amplitudes. (A-C) Compartment size extracted from Pixel-by-pixel fittings of the NOGSE data to Eq. 9, obtained from NOGSE MRI experiments with $N=8$ and T_{NOGSE}=20 ms, and G=28.8 (A) and 57.6 G/cm (B,C). The maps in (A) and (B) are presented in a common scale; (C) is shown in a smaller compartment size scale. **(D)** Compartment size map obtained from conventional PGSE presented in a scale identical to (A) and (B); note that while similar sizes are corroborated by PGSE, the contrast is different from that observed by NOGSE. The experiment shown in (D) was performed with PGSE MRI, Δ/δ = 14.8/5 ms, and the b-values were sampled from 0 to 980 sec/mm^2 in thirteen steps with G_{max}=20 G/cm. A pixel-by-pixel linear fit of the natural logarithm of the PGSE signal against the b-values was performed to obtain the ADC, which was then used to determine the compartment size from $d = \frac{\sqrt{2*ADC*\Delta}}{0.37}$. The 1/0.37 correction factor accounts for a cylindrical geometry.

Figure 6 shows the dependence of the of the *ex-vivo* spinal cord compartment size maps on the number of oscillations, N. The images for N=8 and N=16 (Figures 6A and 6B) exhibit very similar contrasts, with contrast differing slightly when the number of oscillations is further increased to N=32 (Figure 6C). Figures 6D-F show the NOGSE signal dependence in these experiments with increasing x, for the six ROIs defined in Figure 4B. These plots bear two differences compared to the simulations in Figure 2 and the data shown in Figure 3. First, the initial parts of the spinal cord NOGSE signals at low x-values do not begin at identical initial values. This simply reflects our choice of x with respect to the size of the compartments, and is equivalent to beginning the curves shown in Figure 2C at a value larger than zero. More intriguing is the second feature in some of these ROIs: the signal at the initial x values shows a curvature (see for example, ROIs 4 and 6) at $N=8$ and $N=16$. This effect most likely reflects size polydispersity, which tends to shift the dynamic contrast based on the volume fractions of the distribution components (see also Figures 8 and 9 and the 'Discussion' section). Figures 6D-F also show the expected decrease in signal magnitude at the x=y final points of each curve with decreasing number of oscillations, N, for all ROIs. However, the difference between them is lower than for the capillaries' experiments. This evidences the influence of free diffusion effects from water molecules residing in larger pores: for free diffusion, the NOGSE signal exponent at $x = \frac{T_{NOGSE}}{N}$ will behave as $\beta_{NOGSE}^{free}\left(T_{NOGSE}, x = y = \frac{T_{NOGSE}}{N}, N\right) = \beta_{CPMG}^{free}(T_{NOGSE}, N) \propto$

$\left(\frac{T_{NOGSE}}{N}\right)^2$; This N^{-2} dependence is smoother than the linear dependence predicted for the restricted diffusion case: $\beta_{NOGSE}^{restricted}\left(T_{NOGSE}, x = y = \frac{T_{NOGSE}}{N}, N\right) = \beta_{CPMG}^{restricted}(T_{NOGSE}, N) \propto \left(1 - (2N+1)\frac{\tau_c}{T_{NOGSE}}\right)$.

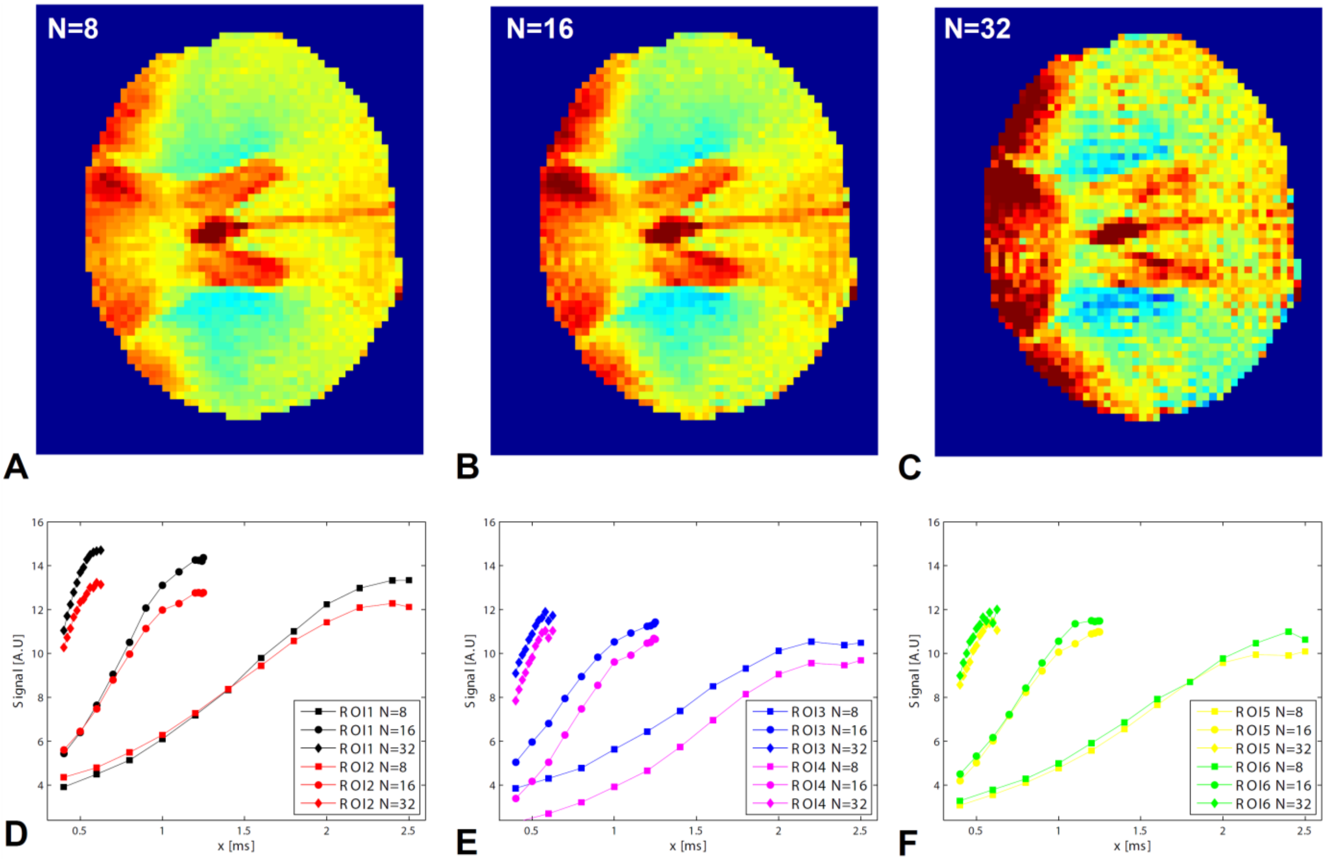

Figure 6. Compartment dimension maps obtained from NOGSE MRI for different *N*. For all experiments, T_{NOGSE}=20 ms, *G*=57.6 G/cm and *N*=8 **(A)** *N*=16 **(B)** and *N*=32 **(C)**. Note that similar contrast is observed for *N*=8 and 16, while slightly different compartment sizes are obtained for *N*=32. **(E-F)** ROI analysis (ROIs are defined in Figure 5B). Note the expected increase in contrast with increasing *N* for all ROIs. Solid lines are guides to the eye for the corresponding experiments. *x* was initialized at x_{min} = 0.4 ms and incremented in twelve steps up to $x_{max} = T_{NOGSE}/N$.

Characterization of WM fibers in terms of compartment size may also be highly important in the brain, where changes in microstructure often reflect different functional properties [49] or pathologies [50]. We explored the possibility of utilizing NOGSE for generating contrast in the WM of the mouse brain targeting specifically the corpus callosum, whose microstructural features are known to vary with location [51,52], and whose orientation was known *a-priori*, facilitating the application of the NOGSE gradient vector in an orientation perpendicular to the main axis of the fibers. The signal evolution in this experiment, shown in Figure 7A, clearly follows the trends outlined above, evidencing an increase of signal with increasing *x*-values. Figure 7B shows the map of compartment sizes of the corpus callosum, overlaid on a T_2 weighted image of the entire brain taken at the same *TE* as the NOGSE experiments. Note the varying contrast between different corpus callosum regions provided by this compartment size-sensitive technique.

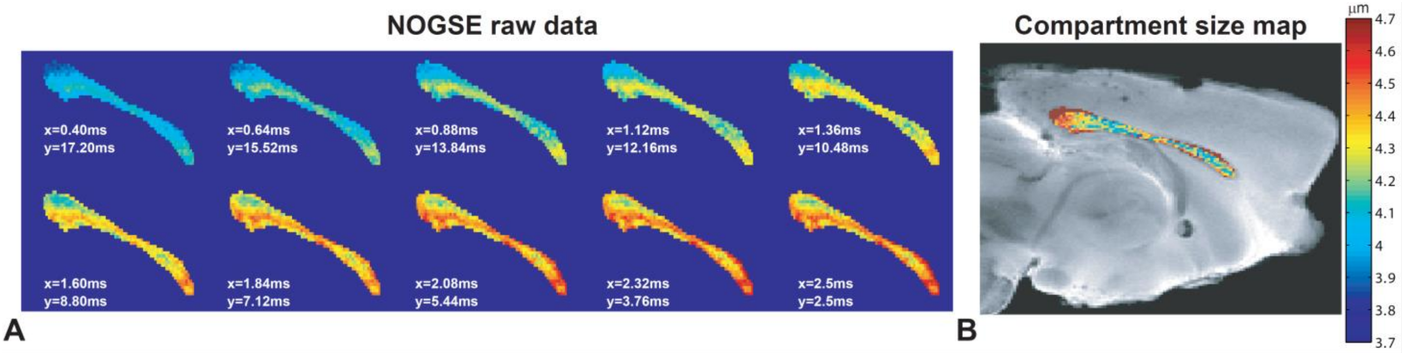

Figure 7. NOGSE MRI in the ex-vivo mouse brain. (A) Raw data from NOGSE MRI in the mouse brain with N=8, G=57.6 G/cm and T_{NOGSE}=20 ms, masked for the corpus callosum. Note the clear signal increase with increasing x. **(B)** Compartment size map obtained from a pixel-by-pixel fit of the data to Eq. 9, overlaid on a T_2 weighted image. The corpus callosum shows distinct regions of varying compartment size. The NOGSE gradient was applied in the direction perpendicular to the main axis of the axons in the corpus callosum; *e.g.*, in the up-down axis of the image.

Discussion

Measuring small compartmental dimensions noninvasively is a primary goal for NMR, especially in biomedical applications where microstructural information may characterize pathological processes [53] or even functional properties such as axonal conduction velocities [54]. PGSE-based approaches have played a decisive role in noninvasively extracting such microstructural information based on deviations of the signal decay from mono-exponential diffusion [55,56]. Interest in time-dependent OGSE-based approaches utilizing oscillating gradients to probe different frequencies in the diffusion spectrum $D(\omega)$ [31] has also developed vigorously in recent years owing to its potential in providing structural information in small pores using rather low gradient amplitudes [16,20,26-29,31,46]. While powerful and useful, the OGSE approach is at its best when the FT of the integral of the applied gradient waveform has a single frequency component and lacks a zero frequency peak around *D(0)*, a requirement that may be experimentally quite demanding [24].

Here we introduced the NOGSE methodology, which employs non-uniform gradient modulations for accurate measurement of compartment sizes. Instead of focusing on an accurate determination of $D(\omega)$ at each particular ω, NOGSE's waveform is designed to generate a signal amplitude modulation that is directly sensitive to the width of $D(\omega) \propto t_c^{-1}$; this method thus provides a more direct and sensitive means for determining restriction lengths. Among the major features of the NOGSE methodology we count: (1) A constant-time, constant-gradient-amplitude diffusion-sensitizing period, possessing multiple frequency components whose relative weights are varied. (2) Whereas OGSE sequences are mostly analyzed in the frequency domain [16,31], NOGSE is performed and analyzed in the time domain*; e.g.*, with increasing *x*. The advantages of a direct time-domain analysis are three-fold: first, they lift OGSE's requirement for a nonzero central component in the gradient's frequency spectrum; second, the transition between free and restricted diffusion regimes is manifest as an amplitude modulation, as opposed to discriminations between transitions from free to restricted diffusion regimes which need to be detected on the basis of smooth transitions in spectral density power laws [30,31]; and third, NOGSE signal increases in a simple fashion as a function of *x* and plateaus once the maximum restriction is achieved, thus emphasizing the restricting effects imposed by the pore boundaries. By contrast, the ADC obtained from each OGSE measurement increases with increasing frequency and plateaus at the free diffusion regime, thus accentuating the free diffusion regime [16,31]. (3) NOGSE's sensitivity to the restriction length (as manifested in NOGSE's amplitude modulation) is very high and varies as l_c^6; were this quantity to be determined from the width of the displacement power spectrum of Eq. 5, as is done in standard approaches, the sensitivity would vary as l_c^4. (5) NOGSE's amplitude modulation will depend on the quantity $\Delta\beta_{NOGSE}^{restricted}(T_{NOGSE}, N) = \frac{1}{4D_0^2}\,(\gamma G)^2 * (N-1)\, l_c^6$, suggesting that N can be utilized towards dynamically amplifying NOGSE's compartment size contrast [41]. This contributes an additional source of sensitivity, especially when considering clinical scanners, which are equipped with relatively weak gradients. Furthermore, at clinical fields, the relatively long T_2 of CNS tissues provides ample time to carry out a large number of oscillations within the diffusion sequence to enhance sensitivity towards compartment size. For a clinical gradient amplitude of 6 G/cm and N=256 at T_{NOGSE}=200 ms, for example, 1.5 and 2 μm compartments will give rise to ~9 and ~25% amplitude modulations, respectively, suggesting that small compartments could be resolved even with weak gradient strengths.

The simulations and phantom tests shown in this study confirmed all of these features, and suggest NOGSE's strong contrasting abilities between small compartment sizes when monodisperse systems are considered. Diffusion-diffraction patterns in PGSE NMR [10,17] or in other methodologies [35,37] are also capable of resolving small size differences; however, for comparison, the first diffusion-diffraction minimum for compartments smaller than 2 μm would only be observed when applying gradient amplitudes exceeding well over 1000 G/cm. Furthermore, high resolution in q is required for resolving small compartments [57], leading in turn to very long experiment durations. By contrast, extracting the compartment size with NOGSE requires few data points; in fact, in simple cases, the first and last points would suffice to fully characterize the amplitude modulation of ΔM_{NOGSE} – especially considering the significant NOGSE signal increases obtained even for small compartments.

Generating MRI contrast based on compartment size is an important challenge for diffusion MRI for segmenting different tracts in normal tissues [8], or when seeking an early detection of pathological conditions [58]. The spinal cord results in Figures 5 and 6 indicate that compartment size contrast can indeed be derived from NOGSE MRI. Moreover, the existence of structural polydispersity could be inferred from the different compartment size maps obtained from different gradient amplitudes; this is not unexpected, as NOGSE will in fact act as a filter enhancing different elements of the size distribution. This feature is reminiscent of recent literature proposing non-uniform gradient pairs numerically tailored towards size-specific sensitivity [32,34]. Further evidence for NOGSE's potential to characterize compartment sizes was noted in the brain NOGSE experiments focusing on the corpus callosum; the signal evolution again followed the expected trends, and a NOGSE-derived compartment size map appeared to segment the corpus callosum into distinct regions, consistent with several recent diffusion MR studies showing marked size-based contrast using PGSE [51,52]. As in the spinal cord specimen, different sizes were obtained for different gradient amplitudes (not shown), suggesting NOGSE's potential for resolving elements of size distributions.

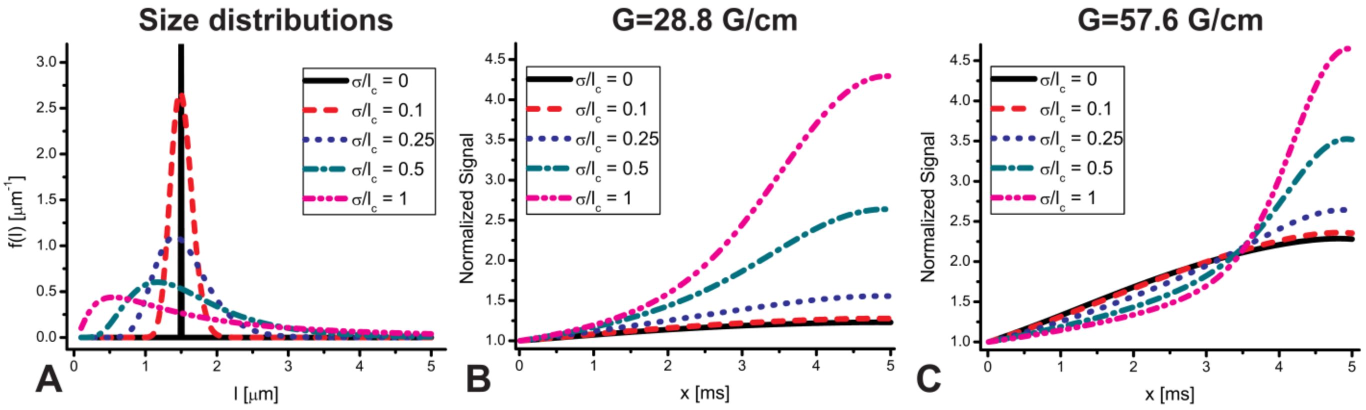

Figure 8. Simulations for NOGSE MR in the presence of size polydispersity for different gradient amplitudes. **(A)** Log-normal size distributions analyzed in this study of the form $f(l) = \frac{1}{l\sigma\sqrt{2\pi}} e^{-\frac{(\ln(l)-\ln(l_c))^2}{2\sigma^2}}$, where l_c is a median length equal to 1.5 μm for all distributions and σ/l_c are as indicated. **(B,C)** NOGSE signal for the corresponding size distributions with G=28.8 and 57.6 G/cm, respectively. Note that at long x, the magnitude of the signal increases with increasing variance of the size

distribution. When stronger gradient amplitudes are applied, the signals depart from their usual monodisperse forms, and a curvature in the signal at lower x can be noticed, corresponding to an attenuation of the larger pores' signal. This sensitivity to size distribution may be utilized to infer on the elements of the distribution. For all simulations, T_{NOGSE}=40 ms, $N=8$ and D_0=0.7*10^{-5} cm^2/sec, and pores were assumed to be cylindrical.

The results from these biological specimens, and especially the different size contrasts obtained upon assaying different gradient amplitudes, merit a brief analysis on the effects of size distributions on the NOGSE signal. Figure 8A shows several log-normal size distributions assumed for this assessment, while Figures 8B and 8C show NOGSE signals simulated for these distributions at G=28.8 and 57.6 G/cm, respectively. Even for a modest distribution of ~25%, the NOGSE signals feature significant changes in signal response: the amplitude of the NOGSE curve increases with increasing size distribution reflecting the increasing fraction of larger pores that are sensitized to the oscillating gradient effects. Furthermore, as the weight of the larger pores increases, the signal at short x begins to acquire a kind of curvature that could also be seen in some of the ROIs in the experiments shown Figures 4 and 6. This reflects the fact that for these long y periods, the signal contribution from the larger pores is very low, and the spins that suffer restriction dominate NOGSE's signal. However, as x increases, the larger pores start to dominate the NOGSE signal. When the gradient increases (Figure 8C), these attributes become even more pronounced. Similar trends are obtained for larger N (data not shown).

Another characteristic of size distributions is shown in Figure 9, where the NOGSE signal is plotted as a function of N for a monodisperse system (panel A) and for a system characterized by a modest size distribution (panel B). The NOGSE signal varies strongly with increasing distributions for all N; however, the general features of the N-dependence are preserved. Such measurements may prove useful for emphasizing specific compartment sizes or even help resolving elements of a size distribution in tissues. These features bode well for NOGSE as a means for resolving different elements of the distribution or sensitizing the signal towards specific compartment sizes.

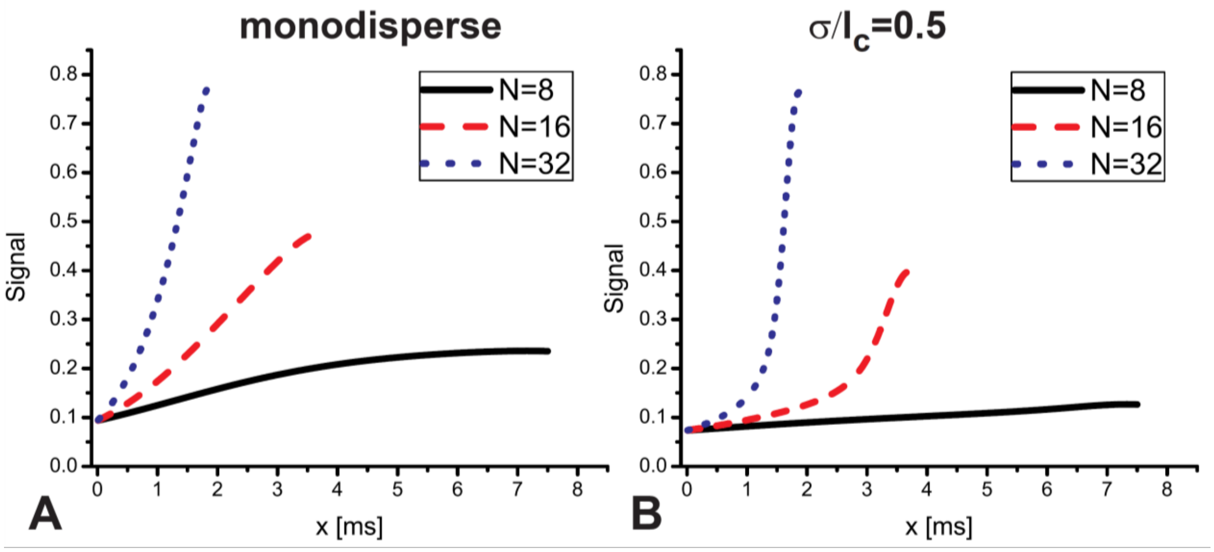

Figure 9. Simulations for NOGSE MR in the presence of size polydispersity for different *N*. (A) The NOGSE signal for a monodisperse system and **(B)** for a modest size distribution characterized by σ/l_c = 0.5 (shown in cyan in Figure 8A). Note that the general trends of the *N* dependence are nearly identical; however, curvatures at lower *x*-values are discernible. For all simulations, T_{NOGSE}=60 ms, *G*=57.6 G/cm and D_0=0.7*10^{-5} cm^2/sec.

The *ex-vivo* NOGSE analyses presented here were based on a number of prior assumptions. First, it was assumed NOGSE gradients were directed perpendicular to the principal orientation of a cylindrically symmetric compartment. While this is a good assumption in white matter it certainly does not hold for gray matter, where a significant fraction of anisotropic compartments may be randomly oriented [59,60]. A related assumption was that all compartments, being cylindrical, are to be corrected by a factor of $d \sim l_c/0.37$; when violated, the apparent compartment size may require a different scaling. The free diffusion coefficient D_0 was also taken as a fixed, known parameter; if unknown, D_0 can be estimated from two NOGSE curves collected at different gradient amplitudes, or from an OGSE-like measurement with very rapid oscillations. The Gaussian Phase Distribution approximation was also assumed valid during the entire T_{NOGSE}, consistent with previous literature [23,42]. We note that in the regimes where this approximation could be broken (e.g., when $G \gg \frac{1}{l_f \gamma T_m}$ where l_f is the mean free path of the moving particles and T_m the gradient's modulation period) Eq. 3 will no longer hold [36,37, 42].

However, we expect that the time scales in which the GPD approximation is broken are not easily achievable in tissues. Finally, we assumed that the NOGSE gradients were rectangular, whereas in the experiments they were trapezoidal. This may have introduced a slight systematic bias to the extracted sizes, although we expect this effect to be quite small [23], especially since NOGSE probes D(ω) by multiple frequencies to detect the transitions between free and restricted diffusion. Indeed, this was corroborated in our phantom experiments, where very accurate sizes were obtained despite that we completely ignored the gradient ramps. Moreover, we observed an excellent agreement between the lengths determined here by the NOGSE sequence shown in Figure 1C and the length determined for the same microcapillaries using the SDR sequence (modulated by refocusing pulses and without ramps) of Fig. 1A [41]. Notice as well that we did not attempt to model the tissue micro-architecture [61]; that is, a single diffusing component and no l_c heterogeneities were assumed. Further modeling of tissue components [62] and their NOGSE signal responses, may result in better characterizations of tissue microstructure. In fact, as the NOGSE gradient blocks are essentially individual gradient vectors, the parameter space for NOGSE variants is indeed large: in analogy to double-PGSE MR [59,63,64] one could implement double-NOGSE in order to probe diffusion correlations in different directions, or one could implement NOGSE in DTI mode to sensitize the measurements towards macroscopic anisotropy and orientation. A further use of NOGSE's ability to interrogate compartment sizes even with just the initial and final points of the curve may prove useful in diffusion f-MRI experiments [65]. The potential of these avenues is currently being tested *in-vivo*.

Conclusions

We have presented a new MR methodology for extracting compartment dimensions of confined diffusing spins, at relatively low gradient amplitudes. The ensuing NOGSE approach draws from dynamical decoupling [38] and selective dynamical recoupling [40,41] concepts, and applies them in the context of diffusion-driven spin evolution. The resulting method achieves a diffusion-imposed signal amplitude modulation that can sensitively discern between confinement sizes. When compared to alternatives available for probing such microstructural information, NOGSE exhibits advantages in terms of lower requirements in its gradient amplitudes, a constant time operation, and a very high dynamic range of compartment size characterization. Analytical descriptions of the NOGSE signal evolution were presented which were fully validated in a robust phantom system where accurate, biologically-relevant compartment sizes were obtained at low gradient amplitudes. NOGSE was also combined with MRI, affording novel maps of compartmental dimensions in both pig spinal cords and mouse brain. These experiments are being extended towards application of the NOGSE methodology in *in-vivo* water and metabolite MR studies for accurate noninvasive measurements of compartment sizes.

Acknowledgements

The authors thank Dr. Nava Nevo (Weizmann Veterinary Services) for her assistance with the brain specimens. This work was supported by an ERC Advanced Grant #246754, a Helen and Martin Kimmel Award for Innovative Investigation, and the generosity of the Perlman Family Foundation. GAA acknowledges the support of the European Commission under the Marie Curie Intra-European Fellowship for Career Development Grant No. PIEF-GA-2012-328605.

Appendix

NOGSE analytical expression for a Lorentzian spectrum $S(\omega)$. We begin by providing a full analytical expression of Eq. (9) under the assumption that the displacement's power spectrum, $S(\omega)$, is dominated by a single Lorentzian term (Eq. 5); further details are given in Ref. [41]. The NOGSE signal is given by

$$M_{NOGSE}(T_{NOGSE}, x, y, N) = M_{CPMG}\big((N-1)x, N-1\big) \times M_{Hahn}(y) \times M_{Cross-NOGSE}(T_{NOGSE}, x, y, N). \tag{A1}$$

The Hahn signal decay is [66,67]:

$$M_{Hahn}(T_{NOGSE}) = \exp\left\{-\gamma^2 G^2 D_0\, \tau_c^2\, T_{NOGSE}\, \left[1 - \frac{\tau_c}{y}\left(3 + \exp\left(-\frac{T_{NOGSE}}{\tau_c}\right) - 4\exp\left(-\frac{T_{NOGSE}}{2\tau_c}\right)\right)\right]\right\}, \tag{A2}$$

the CPMG decay can be written as

$$M_{CPMG}(T_{NOGSE}, N) = \exp\{-\gamma^2 G^2 D_0\, \tau_c^2\, [T_{NOGSE} - \tau_c(A+B)]\}, \tag{A3}$$

with

$$\begin{cases} A = (2N+1) - (-1)^N e^{-\frac{T_{NOGSE}}{\tau_c}}, \\ B = \dfrac{4(-1)^{N+1}}{\left(e^{-\frac{T_{NOGSE}}{N\tau_c}} + 1\right)^2} \left[\begin{array}{c} e^{-\frac{T_{NOGSE}}{\tau_c}}\left(e^{-\frac{3T_{NOGSE}}{2N\tau_c}} + e^{-\frac{T_{NOGSE}}{2N\tau_c}} + e^{-\frac{T_{NOGSE}}{N\tau_c}}\right) + \\ e^{-\frac{3T_{NOGSE}}{2N\tau_c}} + e^{-\frac{T_{NOGSE}}{2N\tau_c}} + Ne^{-\frac{2T_{NOGSE}}{N\tau_c}} + (N-1)e^{-\frac{T_{NOGSE}}{N\tau_c}} \end{array}\right], \end{cases}$$

and finally, the cross-term decay is

$$\begin{aligned} M_{Cross-NOGSE}(T_{NOGSE}, x, y, N) = exp\Bigg\{ -\frac{\gamma^2 G^2 D_0\, \tau_c^2}{\left(e^{\frac{x}{\tau_c}}+1\right)} \Bigg[\Bigg(1 + e^{-\frac{y}{\tau_c}} - 2e^{-\frac{1\,y}{2\tau_c}} - 2e^{\frac{12x-y}{2\ \tau_c}} + e^{\frac{x-y}{\tau_c}} + 4e^{\frac{1x-y}{2\ \tau_c}} - \\ 2e^{\frac{1x-2y}{2\ \tau_c}} - 2e^{\frac{1\,x}{2\tau_c}} + e^{\frac{x}{\tau_c}} \Bigg) + (-1)^N \Bigg(e^{-\frac{xN-x+y}{\tau_c}} - 2e^{-\frac{12xN-2x+y}{2\ \tau_c}} - 2e^{\frac{1-4x+2xN+y}{2\ \tau_c}} + e^{-\frac{-2x+xN+y}{\tau_c}} + \\ 4e^{-\frac{1-3x+2xN+y}{2\ \tau_c}} - 2e^{-\frac{1-3x-2xN+2y}{2\ \tau_c}} + e^{-\frac{(N-1)x}{\tau_c}} - 2e^{-\frac{1x(-3+2N)}{2\ \tau_c}} + e^{-\frac{(N-2)x}{\tau_c}} \Bigg) \Bigg] \Bigg\}. \end{aligned} \tag{A4}$$

For cylinders, it is a good approximation to set $\tau_c = 0.26^2 d^2/D_0$, where d is the cylinder's diameter.

NOGSE analytical expression for more complex geometries. For more complex geometries, including spherical confinements, the displacement power spectrum $S(\omega)$ can be written as a sum of Lorentzian terms

$$S(\omega) = \sum_k \frac{D_0 b_k \tau_k^2}{(1+\tau_k^2\omega^2)\pi}. \tag{A5}$$

The coefficients b_k and correlation times τ_k depend on the geometry of the pores and can be found in Ref. [43] for cylinders, spheres and planar layers. Based on this power spectrum the NOGSE signal will be given now by

$$M(T_{NOGSE}, x, y, N) = \prod_k \left[M_{NOGSE}^k(T_{NOGSE}, x, y, N)\right]^{b_k}, \tag{A6}$$

where $M_{NOGSE}^k(T_{NOGSE}, x, y, N)$ is as described in Eqs. A1-A4 by setting $\tau_c = \tau_k$.

References

[1] Y.Q. Song, Magnetic Resonance of Porous Media (MRPM): A perspective. J. Magn Reson. 229 (2013) 12-24.

[2] P.T. Callaghan, Translational dynamics and magnetic resonance, Oxford University Press (2011).

[3] D.S. Grebenkov, NMR survey of reflected Brownian motion. Rev. Mod. Phys. 79 (2007) 1077-1137.

[4] E.O. Stejskal, J.E. Tanner, Spin diffusion measurements - spin echoes in presence of a time-dependent field gradient. J. Chem. Phys. 42 (1965) 288-292.

[5] P.T. Callaghan, A. Coy, T.P.J. Halpin, D. Macgowan, K.J. Packer, F.O. Zelaya, Diffusion in porous systems and the influence of pore morphology in Pulsed Gradient Spin-Echo Nuclear-Magnetic-Resonance studies. J. Chem. Phys. 97 (1992) 651-662.

[6] Johansen-Berg H., Behrens T.E.J., Diffusion MRI: From quantitative measurement to in-vivo anatomy, (2009) Academic Press.

[7] S. Mori, R. Itoh, J.Y. Zhang, W.E. Kaufmann, P.C.M. van Zijl, M. Solaiyappan, P. Yarowsky, Diffusion tensor imaging of the developing mouse brain. Magn. Reson. Med. 46 (2001) 18-23.

[8] H.H. Ong, A.C. Wright, S.L. Wehrli, A. Souza, E.D. Schwartz, S.N. Hwang, F.W. Wehrli, Indirect measurement of regional axon diameter in excised mouse spinal cord with q-space imaging: Simulation and experimental studies. Neuroimage 40 (2008) 1619-1632.

[9] E.L. Hahn, Spin echoes, Phys. Rev. 80 (1950) 580-594.

[10] P.T. Callaghan, S.L. Codd, J.D. Seymour, Spatial coherence phenomena arising from translational spin motion in gradient spin echo experiments. Concepts Magn. Reson. 11 (1999) 181-202.

[11] N. Shemesh, E. Ozarslan, P.J. Basser, Y. Cohen, Detecting diffusion-diffraction patterns in size distribution phantoms using double-pulsed field gradient NMR: Theory and experiments. J. Chem. Phys. 132 (2010) 034703.

[12] P.P. Mitra, P.N. Sen, L.M. Schwartz, Short-time behavior of the diffusion-coefficient as a geometrical probe of porous-media. Phys. Rev. B 47 (1993) 8565-8574.

[13] P.N. Sen, Time-dependent diffusion coefficient as a probe of geometry. Concepts Magn. Reson. Part A 23A (2004) 1-21.

[14] Y. Assaf, T. Blumenfeld-Katzir, Y. Yovel, P.J. Basser, AxCaliber: A method for measuring axon diameter distribution from diffusion MRI. Magn. Reson. Med. 59 (2008) 1347-1354.

[15] Y.Q. Song, S.G. Ryu, P.N. Sen, Determining multiple length scales in rocks. Nature 406 (2000) 178-181.

[16] J.C. Gore, J.Z. Xu, D.C. Colvin, T.E. Yankeelov, E.C. Parsons, M.D. Does, Characterization of tissue structure at varying length scales using temporal diffusion spectroscopy. NMR Biomed. 23 (2010) 745-756.

[17] A. Bar-Shir, L. Avram, E. Ozarslan, P.J. Basser, Y. Cohen, The effect of the diffusion time and pulse gradient duration ratio on the diffraction pattern and the structural information estimated from q-space diffusion MR: Experiments and simulations. J. Magn Reson. 194 (2008) 230-236.

[18] J. Stepisnik, Analysis of NMR self-diffusion measurements by A density-matrix calculation. Physica B & C 104 (1981) 350-364.

[19] P.T. Callaghan, J. Stepisnik, Frequency-Domain analysis of spin motion using modulated-gradient NMR. J. Magn. Reson. A 117 (1995) 118-122.

[20] M. Schachter, M.D. Does, A.W. Anderson, J.C. Gore, Measurements of restricted diffusion using an oscillating gradient spin-echo sequence. J. Magn. Reson. 147 (2000) 232-237.

[21] D. Topgaard, C. Malmborg, O. Soderman, Restricted self-diffusion of water in a highly concentrated W/O emulsion studied using modulated gradient spin-echo NMR. J. Magn. Reson. 156 (2002) 195-201.

[22] E.C. Parsons, M.D. Does, J.C. Gore, Temporal diffusion spectroscopy: Theory and implementation in restricted systems using oscillating gradients. Magn. Reson. Med. 55 (2006) 75-84.

[23] A. Ianus, B. Siow, I. Drobnjak, H. Zhang, D.C. Alexander, Gaussian phase distribution approximations for oscillating gradient spin echo diffusion MRI. J. Magn. Reson. 227 (2013) 25-34.

[24] E.C. Parsons, M.D. Does, J.C. Gore, Modified oscillating gradient pulses for direct sampling of the diffusion spectrum suitable for imaging sequences. Magn. Reson. Imaging 21 (2003) 279-285.

[25] D.C. Colvin, T.E. Yankeelov, M.D. Does, Z. Yue, C. Quarles, J.C. Gore, New insights into tumor microstructure using temporal diffusion spectroscopy. Cancer Res. 68 (2008) 5941-5947.

[26] J.Z. Xu, M.D. Does, J.C. Gore, Dependence of temporal diffusion spectra on microstructural properties of biological tissues. Magn. Reson. Imaging 29 (2011) 380-390.

[27] M.D. Does, E.C. Parsons, J.C. Gore, Oscillating gradient measurements of water diffusion in normal and globally ischemic rat brain. Magn. Reson. Med. 49 (2003) 206-215.

[28] J.Z. Xu, K. Li, R.A. Smith, J.C. Waterton, P. Zhao, H.D. Chen, M.D. Does, H.C. Manning, J.C. Gore, Characterizing Tumor Response to Chemotherapy at Various Length Scales Using Temporal Diffusion Spectroscopy. PloS One 7 (2012) e41714.

[29] M. Aggarwal, M.V. Jones, P.A. Calabresi, S. Mori, J.Y. Zhang, Probing mouse brain microstructure using oscillating gradient diffusion MRI. Magn. Reson. Med. 67 (2012) 98-109.

[30] S. Lasic, J. Stepisnik, A. Mohoric, Displacement power spectrum measurement by CPMG in constant gradient. J. Magn. Reson. 182 (2006) 208-214.

[31] J. Stepisnik, S. Lasic, A. Mohoric, I. Sersa, A. Sepe, Spectral characterization of diffusion in porous media by the modulated gradient spin echo with CPMG sequence. J. Magn. Reson. 182 (2006) 195-199.

[32] I. Drobnjak, B. Siow, D.C. Alexander, Optimizing gradient waveforms for microstructure sensitivity in diffusion-weighted MR. J. Magn. Reson. 206 (2010) 41-51.

[33] I. Drobnjak, H. Zhang, M.G. Hall, D.C. Alexander, The matrix formalism for generalised gradients with time-varying orientation in diffusion NMR. J. Magn. Reson. 210 (2011) 151-157.

[34] B. Siow, I. Drobnjak, A. Chatterjee, M.F. Lythgoe, D.C. Alexander, Estimation of pore size in a microstructure phantom using the optimised gradient waveform diffusion weighted NMR sequence. J. Magn. Reson. 214 (2012) 51-60.

[35] F.B. Laun, T.A. Kuder, W. Semmler, B. Stieltjes, Determination of the defining boundary in Nuclear Magnetic Resonance diffusion experiments. Phys. Rev. Lett. 107 (2011) 048102.

[36] F.B. Laun, T.A. Kuder, A. Wetscherek, B. Stieltjes, W. Semmler, NMR-based diffusion pore imaging. Phys. Rev. E 86 (2012).

[37] N. Shemesh, C.F. Westin, Y. Cohen, Magnetic Resonance Imaging by synergistic diffusion-diffraction patterns. Phys. Rev. Lett. 108 (2012) 058103.

[38] G.S. Uhrig, Keeping a quantum bit alive by optimized pi-pulse sequences. Phys. Rev. Lett. 98 (2007) 100504.

[39] E.R. Jenista, A.M. Stokes, R.T. Branca, W.S. Warren, Optimized, unequal pulse spacing in multiple echo sequences improves refocusing in magnetic resonance. J. Chem. Phys. 131 (2009) 204510.

[40] P.E.S. Smith, G. Bensky, G.A. Alvarez, G. Kurizki, L. Frydman, Shift-driven modulations of spin-echo signals. Proc. Nat. Acad. Sci. U.S.A. 109 (2012) 5958-5961.

[41] G.A. Alvarez, N. Shemesh, L. Frydman, Coherent dynamical recoupling of diffusion-driven decoherence in magnetic resonance, Phys. Rev. Lett. 111 (2013) 080404 (1-6).

[42] J. Stepisnik, Validity limits of Gaussian approximation in cumulant expansion for diffusion attenuation of spin echo. Physica B 270 (1999) 110-117.

[43] J. Stepisnik, Time-dependent self-diffusion by NMR spin-echo. Physica B 183 (1993) 343-350.

[44] A. Ajoy, G.A. Alvarez, D. Suter, Optimal pulse spacing for dynamical decoupling in the presence of a purely dephasing spin bath. Phys. Rev. A 83 (2011) 032303.

[45] G.A. Alvarez, D. Suter, Measuring the spectrum of colored noise by dynamical decoupling. Phys. Rev. Lett. 107 (2011) 230501.

[46] J. Xu, M.D. Does, J.C. Gore, Sensitivity of MR diffusion measurements to variations in intracellular structure: effects of nuclear size. Magn. Reson. Med. 61 (2009) 828-833.

[47] S. Hertel, M. Hunter, P. Galvosas, Magnetic resonance pore imaging, a tool for porous media research. Phys. Rev. E 87 (2013) 030802.

[48] H.H. Ong, F.W. Wehrli, Quantifying axon diameter and intra-cellular volume fraction in excised mouse spinal cord with q-space imaging. Neuroimage 51 (2010) 1360-1366.

[49] J.A. Perge, J.E. Niven, E. Mugnaini, V. Balasubramanian, P. Sterling, Why do axons differ in caliber? J. Neurosci. 32 (2012) 626-638.

[50] R. Nashmi, M.G. Fehlings, Changes in axonal physiology and morphology after chronic compressive injury of the rat thoracic spinal cord. Neuroscience 104 (2001) 235-251.

[51] D.C. Alexander, P.L. Hubbard, M.G. Hall, E.A. Moore, M. Ptito, G.J.M. Parker, T.B. Dyrby, Orientationally invariant indices of axon diameter and density from diffusion MRI. Neuroimage 52 (2010) 1374-1389.

[52] D. Barazany, P.J. Basser, Y. Assaf, In vivo measurement of axon diameter distribution in the corpus callosum of rat brain. Brain 132 (2009) 1210-1220.

[53] M.D. Budde, J.A. Frank, Neurite beading is sufficient to decrease the apparent diffusion coefficient after ischemic stroke. Proc. Nat. Acad. Sci. U.S.A. 107 (2010) 14472-14477.

[54] S. Cullheim, Relations Between Cell Body Size, Axon Diameter and Axon Conduction-Velocity of Cat Sciatic Alpha-Motoneurons Stained with Horseradish-Peroxidase. Neurosci. Lett. 8 (1978) 17-20.

[55] P.W. Kuchel, A. Coy, P. Stilbs, NMR "diffusion-diffraction" of water revealing alignment of erythrocytes in a magnetic field and their dimensions and membrane transport characteristics. Magn. Reson. Med. 37 (1997) 637-643.

[56] Y. Assaf, D. Ben-Bashat, J. Chapman, S. Peled, I.E. Biton, M. Kafri, Y. Segev, T. Hendler, A.D. Korczyn, M. Graif, Y. Cohen, High b-value q-space analyzed diffusion-weighted MRI: Application to multiple sclerosis. Magn. Reson. Med. 47 (2002) 115-126.

[57] J. Latt, M. Nilsson, C. Malmborg, H. Rosquist, R. Wirestam, F. Stahlberg, D. Topgaard, S. Brockstedt, Accuracy of q-space related parameters in MRI: Simulations and phantom measurements. IEEE Trans. Med. Imaging 26 (2007) 1437-1447.

[58] J.A. Farrell, S.A. Smith, E.M. Gordon-Lipkin, D.S. Reich, P.A. Calabresi, P.C. van Zijl, High b-value q-space diffusion-weighted MRI of the human cervical spinal cord in vivo: feasibility and application to multiple sclerosis. Magn. Reson. Med. 59 (2008) 1079-1089.

[59] N. Shemesh, Y. Cohen, Microscopic and compartment shape anisotropies in gray and white matter revealed by angular bipolar double-PFG MR. Magn. Reson. Med. 65 (2011) 1216-1227.

[60] N. Shemesh, D. Barazany, O. Sadan, L. Bar, Y. Zur, Y. Barhum, N. Sochen, D. Offen, Y. Assaf, Y. Cohen, Mapping apparent eccentricity and residual ensemble anisotropy in the gray matter using angular double-pulsed-field-gradient MRI. Magn. Reson. Med. 68 (2012) 794-806.

[61] T.E.J. Behrens, M.W. Woolrich, M. Jenkinson, H. Johansen-Berg, R.G. Nunes, S. Clare, P.M. Matthews, J.M. Brady, S.M. Smith, Characterization and propagation of uncertainty in diffusion-weighted MR imaging. Magn. Reson. Med. 50 (2003) 1077-1088.

[62] Y. Assaf, P.J. Basser, Composite hindered and restricted model of diffusion (CHARMED) MR imaging of the human brain. Neuroimage 27 (2005) 48-58.

[63] P.P. Mitra, Multiple wave-vector extensions of the NMR Pulsed-Field-Gradient spin-echo diffusion measurement. Phys. Rev. B 51 (1995) 15074-15078.

[64] M.A. Koch, J. Finsterbusch, Compartment size estimation with double wave vector diffusion-weighted Imaging. Magn. Reson. Med. 60 (2008) 90-101.

[65] D. Le Bihan, Looking into the functional architecture of the brain with diffusion MRI. Nat. Rev. Neurosci. 4 (2003) 469-480.

[66] C.F. Hazelwood, D.C. Chang, B.L. Nichols, D.E. Woessner, Nuclear Magnetic-Resonance transverse relaxation-times of water protons in skeletal-muscle. Biophy. J. 14 (1974) 583-606.

[67] R.P. Kennan, J.H. Zhong, J.C. Gore, Intravascular susceptibility contrast mechanisms in tssues. Magn. Reson. Med. 31 (1994) 9-21.